Accepted manuscript. For the open access version please visit: https://doi.org/10.1016/j.robot.2025.105222

Finger Flow: Reactive Reach-while-Grasp Generation for Robotic Arms with Multi-Fingered Hands

Xuming Meng^{a,b}, Henry Maurenbrecher^a, Alin Albu-Schäffer^{a,b}, Manuel Keppler^a

^aGerman Aerospace Center (DLR), Robotics and Mechatronics Center (RMC), Münchener Str. 20, Weβling, 82234, Germany ^bTechnical University of Munich, TUM School of Computation, Information and Technology, Boltzmannstraβe 3, Garching, 85748, Germany

Abstract

Humans effortlessly grasp both stationary and moving objects in one-shot motions, fluidly adapting to disturbances and automatically recovering from failed attempts. In contrast, robots with multi-fingered hands often rely on pre-planned, sequential "reachthen-grasp" strategies, which result in slow, unnatural motions and restrict the robot's ability to react dynamically to changes in the object's location. Moreover, open-loop execution oftentimes leads to grasp failures. To address these challenges, we introduce Finger Flow (FF), a reactive motion generator that uses the visual feedback from an onboard camera and position feedback from fingers and arms to robustly reach and grasp stationary and moving objects with unpredictable behavior. During the reaching, FF continuously guides the hand to avoid finger-object collisions and adjusts the hand's reactive opening and closure based on its relative position to the object. This state-dependent behavior results in automatic recovery from failed grasp attempts. We also provide formal guarantees of convergence and collision avoidance for stationary spherical objects. We evaluate FF on the DLR humanoid robot *neoDavid*, equipped with a multi-fingered hand, and quantitatively assess its performance in a series of grasping experiments involving fast and reactive grasping of a stationary or unpredictable spatially moving object. Running in a closed loop at 3 kHz, FF achieves an 87 % grasp success rate on the stationary object placed at random positions over 130 attempts. Interactive and adversarial human-to-robot handover experiments further demonstrate the robustness and effectiveness of FF.

Keywords: Reactive and sensor-based planning, vision and sensor-based control, grasping, multifingered hands

1. Introduction

Dynamic and reactive reaching and grasping is essential for achieving robust and fluid robotic manipulation, with key objectives including 1) enabling the ability to grasp moving objects [1], 2) increasing grasp success rates by incorporating reactive features to handle perturbations in object and robot states [2], and 3) facilitating natural human-robot interactions through strategies like grasping while reaching, such as dynamic object handovers [3]. Achieving these capabilities requires reliable mechatronics, fast sensing and control [4], and computation-efficient online planning [5, 6], enabling the robot to adapt to external perturbations and changes in the object's state in real-time.

Traditional robotic grasping systems typically operate within a "sense-plan-act" paradigm [7], as noted by both [8] in 1992 and [6] in 2022. This approach executes grasping in two distinct sequential stages: the arm moves toward the object's vicinity (i.e., the grasp pose), and then the fingers close to secure the grasp. Controllers execute two time-dependent trajectories in an open-loop fashion, e.g., sampling-based motion planners [9] ensure collision-free arm movement toward the grasp pose, followed by time-interpolated or optimized finger motions toward their target configuration. Event-triggered logic manages the transition between these actions. However, this sequential approach frequently results in grasp failures when unexpected perturbations affect either the object or robot, necessitating rapid

adaptation or planning to the new grasp goal poses.

While real-time grasp pose generation, including grasp finger configuration, has achieved impressive performance [10, 11, 12], running hand-arm systems from parallel-jaw grippers to 15-DoF multi-fingered hands at up to 50 Hz in real-world hardware, significant challenges remain in the online planning to a continuously changing grasp pose.

Challenge 1: Fast online reaching planning for arms

Existing approaches to online reaching and grasping of moving objects primarily focus on predictable motion patterns. For instance, [13] employs online inference of a pre-trained Recurrent Neural Network (RNN) to predict trajectories of objects moving in linear, circular, or sinusoidal paths, enabling reactive arm control. Alternatively, dynamical system (DS)-based methods generate reaching motions toward online-estimated object poses, as demonstrated in [14] and [15], which achieve interception of objects in predictable motion. Since such trajectories, governed by gravity and air resistance, are inherently predictable, interception points can often be estimated early from limited visual observations.

However, these methods fail when object motion is unpredictable or externally influenced, where long-term forecasting becomes unreliable. In such cases, real-time feedback control is essential. A common approach is Position-Based Visual Servoing (PBVS) [16], which computes end-effector velocity as a proportional response to the pose error between current and

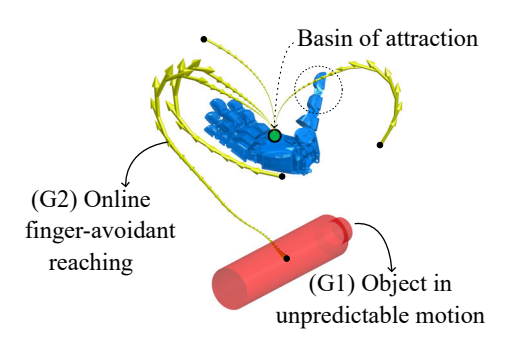


Figure 1: From a hand-centric perspective, the reactive reaching motion can be viewed as guiding an object displaying unpredictable motion toward an attractor, where it eventually settles within the basin of attraction (green dot) while avoiding fingers and palm.

desired configurations. PBVS acts as a local planner, guiding the arm toward updated grasp poses, typically in a straight-line trajectory when orientation is fixed.

Despite its simplicity and real-time capability, PBVS has critical limitations. It does not account for the geometric configuration of the end-effector or potential collisions between fingers and the object during approach. Consequently, it assumes a collision-free path, which is often invalid for dexterous, multi-fingered hands. When the initial end-effector pose is poorly conditioned, finger-object collisions may occur before grasp completion, leading to failure. Recovery typically requires reactive re-planning, which is computationally demanding, especially for high-degree-of-freedom hands with complex mesh geometries. Recent reinforcement learning approaches have shown promise in the reactive grasping of static objects using complex hands, such as the Allegro hand on a Kuka iiwa arm [17]. However, these methods have not been demonstrated in scenarios involving spatially moving, unpredictably maneuvering objects. Reactive strategies utilizing fingertip proximity sensing enable rapid, reflex-like responses to near-contact events. Such approaches have achieved robust grasping and interception of moving or uncertain objects through optical or infrared sensing and integrated finger-arm control [18, 19, 20, 21, 22]. These tactile reflexes complement arm-level feedback, improving grasp reliability in unpredictable environments.

Efficient real-time motion generation remains a key challenge. While methods such as artificial potential fields [23, 24], global elastic bands [25], navigation functions [26, 27], circular vector fields [28, 29], and DS-based controllers [30, 31, 32] offer computationally efficient, closed-form solutions for navigation and manipulator control, they are typically designed for simplified end-effectors or 7-DOF arms. A unified, reactive control framework that integrates real-time object pose feedback, finger-aware fast reactive reaching planning for unpredictable spatially moving objects is still lacking.

Challenge 2: Finger-arm coordination in fluid grasping and reaching

Human studies reveal a tightly coupled relationship between arm reaching and finger closing during dynamic manipulation

tasks [33], where hand aperture evolves smoothly in coordination with arm motion. This natural synergy enables efficient, fluid reach-and-grasp behaviors even under uncertainty. Inspired by this, [6] employed deep reinforcement learning (RL) to generate end-to-end policies that jointly control 6-DoF handbase pose and 19-DoF finger configurations in a single motion sequence. While promising, the underlying coordination mechanism, how arm motion and finger closing influence each other, remains poorly understood, and the transfer of such policies to real-world hardware is hindered by sim-to-real gaps, such as computational bottlenecks in deep RL and sensitivity to perturbations on objects. As a result, most practical systems still rely on sequential coordination strategies, where finger closure is triggered only after specific conditions are met during arm motion. Time-based triggers require precise synchronization between the arm trajectory and low-latency gripper actuation [14, 1], making them fragile to delays or disturbances. Distance-based triggers, in contrast, initiate the closing action when the object enters a predefined proximity zone relative to the gripper [13], as seen in parallel-jaw grippers. Such decoupled strategies lack the geometric awareness needed to prevent collisions between fingers and objects during approach, especially when reaching toward fast-moving targets.

Challenge 3: Maximizing grasp success despite sensing uncertainties and execution errors

For multi-fingered hand-arm systems, robustness to sensing noise and actuation errors is critical, particularly when grasping dynamic objects. Insights can be drawn from industrial assembly tasks, where utilizing objects' or environments' shape compensates for imprecision. The *bean-bowl* model [34] illustrates this principle: inserting a peg into a hole is analogous to dropping a bean into a convex bowl, where the bowl's inner contours, the "Attraction Region in Environment", guide the object to the target through passive forces like gravity and friction. This allows successful insertion even with significant misalignment, reducing the need for perfect state estimation.

Instead of relying solely on precise pose estimation, systems can exploit object and hand geometry to create passive or active constraints that tolerate uncertainty. Recent work by [35] advances this idea by using time-varying robot configurations to form dynamic caging constraints—topological enclosures that prevent object escape without requiring full immobilization or accurate state knowledge. Caging refers to immobilizing the object [36], and potentially increases grasp success rate under partial observability and execution errors, making it highly suitable for grasping moving or poorly sensed objects. While caging offers topological robustness, integrating such constraints imposed by high-DoF hands into online motion planning remains an open problem.

Research Gaps

As a summary, we identify the following research gaps:

(G1) Grasping unpredictably moving objects in free space: To the best of the authors' knowledge, no existing approaches demonstrate dynamic grasping of objects with

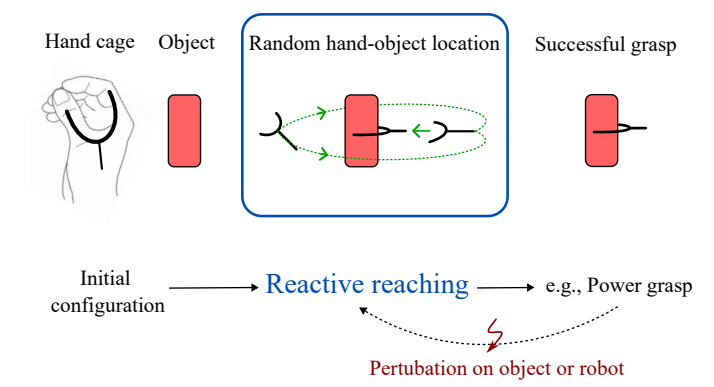


Figure 2: Finger Flow: achieving grasp-while-reaching behavior. The fingers form a U-shaped cage (adapted from [37, Fig. 3]) during reaching.

unpredictable motion in free space using a multi-fingered hand-arm system;

(G2) A computationally efficient geometric abstraction for high-DoF hands enabling real-time finger-avoidant reaching: While complex meshes of multi-fingered hands hinder planning speed, there is no lightweight geometric representation that supports fast, online finger-avoidant reaching.

These two gaps are visualized in Figure 1 in the context of a reach-while-grasp task.

1.1. Our Approach and Contributions

We introduce a motion generation framework to address (G1) and (G2) for the objects with spherical or cylindrical shapes. These two object categories serve as foundational building blocks for several reasons: (1) they encompass a wide range of convex objects that can be effectively approximated through a single spherical or ellipsoidal hull, and (2) they enable rigorous investigation of convergence and collision-avoidance for reaching motion while maintaining analytical tractability. At the end of Section 6.5, we outline the possible roadmap to generalize to more complex shapes as the remaining challenges for future work. We adopt three core design ideas to address (G1) and (G2) as follows.

(I1) Unidirectional object-to-finger-to-arm coordination

To address (G1), fingers and arms must be coordinated. Studies on human prehension show that finger movements precede and guide arm trajectory adjustments during reaching [38, 39]. Inspired by this, we implement a finger motion generator that modulates opening and closing based solely on the distance between the object and an attractor fixed on the palm, adapting automatically to approach speed. Simultaneously, a hand motion generator uses both object state and finger position to dynamically adjust the reaching trajectory. This creates a unidirectional object–finger–arm coordination, enabling arm motion to adapt naturally to finger configuration and object state without explicit synchronization.

(I2) Hand cage: Maximization of success under uncertainty

Learning from [34], one important idea to address (G1) is allowing sub-optimal grasps under execution and perception uncertainty instead of always perusing globally optimal but fragile grasps¹ in a dynamic scenario. A human hand can be considered as naturally forming a "hand cage". A viable strategy is to pre-configure fingers to form a cage, a semi-open space that cages the objects when the arm approaches the object. From a hand-centric perspective, the reaching and grasping motion can be regarded as if the object is guided toward the attractor and ultimately lands in the basin of attraction, see Figure 1. The process of establishing a stable grasp can be realized by the finger closing progressively as the object approaches this attractor, i.e., a smooth transition from a caging configuration—such as a U-shaped hand envelope—to a wrap grasp (e.g., power grasp), cf. Figure 2.

(13) Hand hull: for fast finger collision avoidance

To address (G2), we propose a single continuous fingerdependent hand hull, a computationally efficient mesh representation, particularly well-suited for multi-fingered hands with high degrees of freedom and complex geometries. This hand hull serves as an essential surrogate that encodes the geometries of fingers and palm in current configurations or poses, enabling real-time hand motion generation as outlined in (I1).

Combining these three key ideas, the whole framework contributes the following:

- Finger Flow (FF), a motion generator that implements core ideas (I1) to (I3). The whole framework achieves an execution frequency of more than 3 kHz on low-power mobile CPUs (Intel Core i7-1185G7 @ 3.0 GHz).
- 2) Formal guarantees of both convergence and finger collision avoidance for reaching stationary spherical objects.
- 3) Real-world experiments on the DLR robot *neoDavid* [41]: performing over 130 reaching trials for grasping a stationary tabletop object; dynamic grasping a unpredictably moving cylindrical bottle in free space with over 0.7 m/s median object peak velocity in multiple trials; and also achieves 58 times seamless dynamic human-to-robot object handovers, handling both cooperative and adversarial interaction scenarios throughout the entire reaching and grasping phase.
- Quantitative comparison with PBVS and open-loop FF in simulation; simulation studies for varying hand hull parameters, cylindrical object's size, and surface roughness.

The paper is organized as follows. Section 2 provides an overview of the proposed framework. Section 3 introduces the concept of the hand hull, which serves as the foundation for Section 4, where the first thread, the hand motion generation, is presented. The second thread, finger motion generation, is detailed in Section 5. Section 6 validates our approach through

^{1&}quot;Fragile grasps" refer to the grasps that fulfill quasi-static conditions, e.g., force closure [40], which may fail in a dynamic scenario.

real-world experiments on the DLR robot *neoDavid*, discussions of the experimental results with a simulation study. Finally, we conclude our work in Section 7.

2. Framework Overview

We outline the reaching and grasping strategy adopted in this work and give a brief overview of the whole framework. Figure 3 illustrates the overall framework, which comprises three major blocks that receive feedback from the robot and the camera.

(1) Visual tracker

A visual object tracker that utilizes the estimates the relative position and orientation between the object and the hand in real-time at 30 Hz, refer to [45]. This feedback is essential for the subsequent motion generator.

(2) Finger Flow - Reactive grasping motion generator

The **Hand Motion Thread** leverages the current finger joint positions, 6D hand pose data, and object pose feedback to compute the body velocity for the hand (as detailed in Section 4). This ensures the hand's collision-free motion as it approaches the object. Simultaneously, the **Finger Motion Thread** generates adaptive finger movements (as described in (I1) detailed in Section 5) based on the obtained object-palm relative distance from visual pose estimation. The resulting finger joint position references are then relayed to the finger controller for execution. This subsystem operates with two parallel threads running at a frequency of 3 kHz.

(3) Motion Controller

This module receives the reference joint position trajectories for the finger control [44] and the reference body velocity for the arm control [42, 43]. By left-multiplying the inverse of the body Jacobian with the computed body velocity, the arm joint velocity reference is derived and subsequently transmitted to the arm motion controller. These two controllers translate the references into joint torque commands, which are sent to the motors.

Remark 1. The "Generate grasp" block is not part of this work's contribution. Throughout the work, we assume the desired finger joint position (representing power grasp) and the object-to-hand position and orientation to be given. For guidance on model-based or data-driven grasp pose synthesis, the reader is referred to existing works such as [46, 47].

2.1. Notation

Bold lowercase letters represent vectors, while bold uppercase letters denote matrices. Additionally, a left superscript, such as $^{\mathcal{H}}(\cdot)$, indicates the reference frame in which a vector or an orientation SO(3) or a SE(3) pose is expressed.

3. Hand Hull: A Simplified Hand Mesh

Our goal is to derive a computationally efficient yet accurate mesh approximation for hand reaching generation, facilitating real-time object-finger collision avoidance during the approaching motion. Given that fingers, which are fixed to the palm, can be modeled as primitive shapes organized in several tree structures, we propose a single continuous 3D hull that serves as an obstacle. In the following sections, we consider the following assumption for the object

Assumption 1. The object is a sphere and has a radius of r_o .

3.1. 2D Hand Hull

To illustrate this concept, we give an example of approximating planar fingers using a single 2D hull.

Approximation of planar fingers through primitive shapes. Consider two planar fingers with the object assumed to be a circle with a radius of r_0 under Assumption 1, see Figure 4 (a). Each finger consists of three types of primitive shapes: ellipses, rectangles, and sectors, which are used for the approximation of fingertips, finger links/palms, and junctions, respectively, see Figure 4 (b). The primitive shapes are organized in a tree structure receiving the current finger joint's angle feedback. The width and length of each finger segment are designed to ensure that the hull adequately covers the original hand mesh while minimizing hollow areas between the hull and the actual hand mesh; see the detailed illustrations of the finger segment's approximations in Section Appendix A.

2D Hull: Approximation via an extended hull. To further streamline the process of determining the intersection area between the circular object and the primitive shapes representing the fingers, we reformulate the problem as a hull extension with a specified thickness (as illustrated in Figure 4 (c)) with Assumption 1. Under this reformulation, the object is approximated as a point.

This simplification facilitates the design of the vector flow that guides the object to the attractor (indicated by the green dot in Figure 4 (c)). The guiding vector field design, which underpins this process, will be elaborated upon in Section 4.

3.2. 3D Hand Hull

The concept of planar fingers represents an idealized simplification wherein two fingers are presumed to operate within the same plane. In contrast, multi-fingered hands exhibit more complex kinematics owing to their anthropomorphic design, including fingers' non-planar arrangement with a higher number of degrees of freedom.

Despite this increased complexity, the simplified 2D hand hull can still be effectively employed to construct a three-dimensional hull. Drawing inspiration from rotationally axial symmetric cone structures, we propose a 3D hand hull to cover the whole hand, see Figure 5.

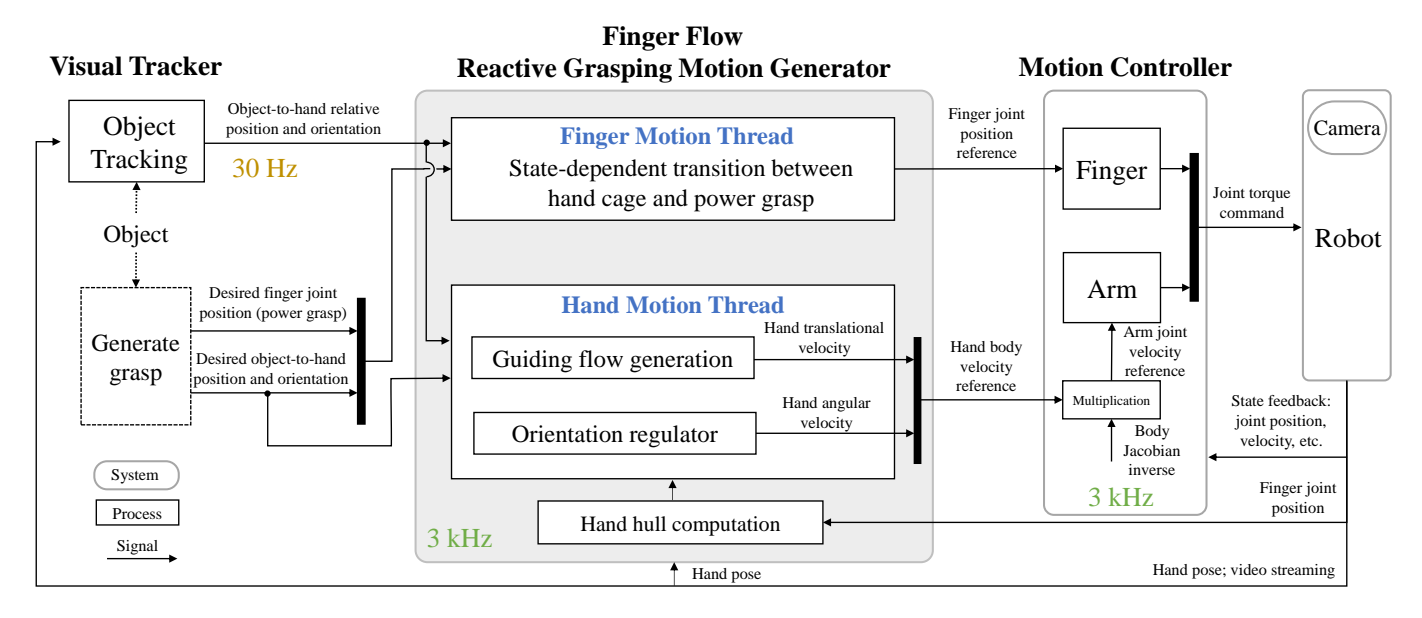


Figure 3: The block diagram of Finger Flow (FF) framework, where the middle block is the main contribution. In Motion Controller: [42, 43] are used for arm control, [44] for finger control; In Visual Tracker, [45] is implemented for object pose visual tracking.

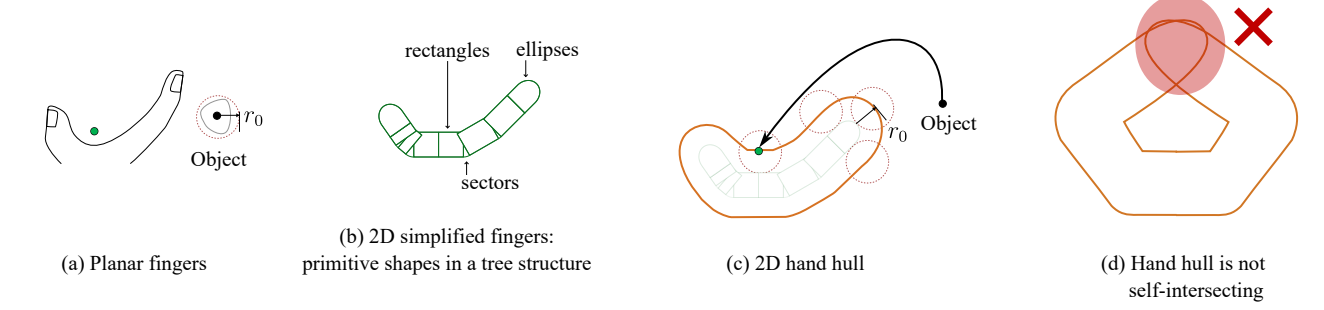


Figure 4: 2D Hand hull in a nutshell. (a): Planar fingers and a circular object with the radius r_0 . (b): The fingers are simplified with primitive shapes (e.g., ellipses, rectangles, circles) (c): The extended hand hull includes the object's radius r_0 . (d): The hull is not self-intersecting when two fingers cross.

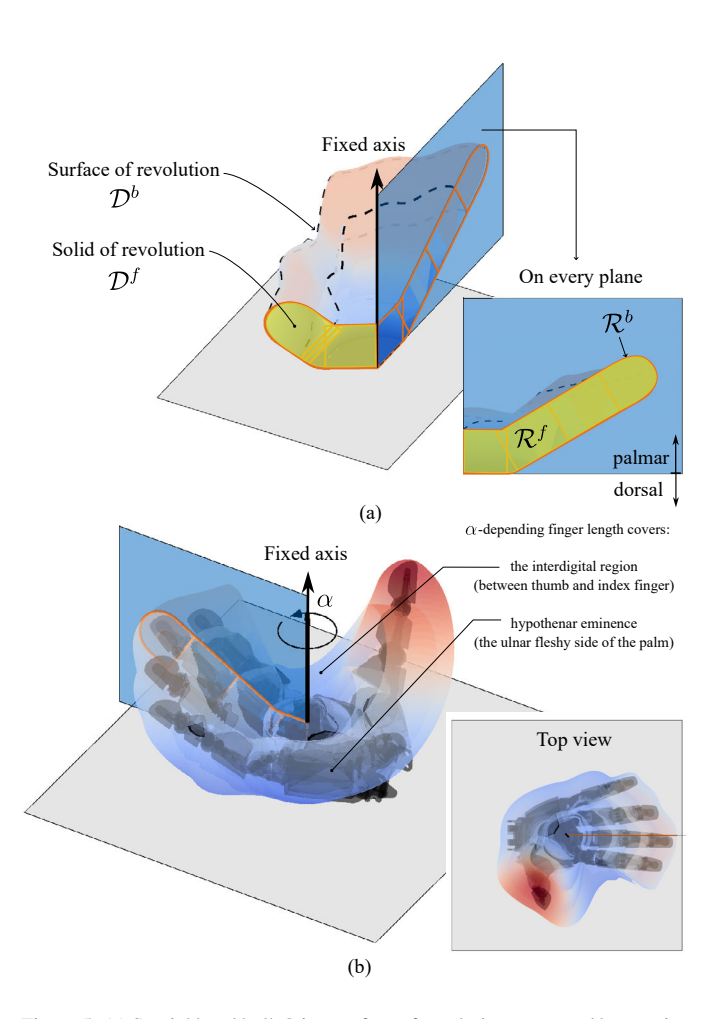


Figure 5: (a) Spatial hand hull \mathcal{D} is a surface of revolution generated by rotating a rotation-angle-dependent 2D kinematics tree (as a generatrix) around a fixed axis. Definitions of regions inside and on the hand hull are depicted. (b) A full presentation of the surface of revolution by rotating the plane 2π around the fixed axis. The color map encodes the height change of the hand hull in the direction fix-axis.

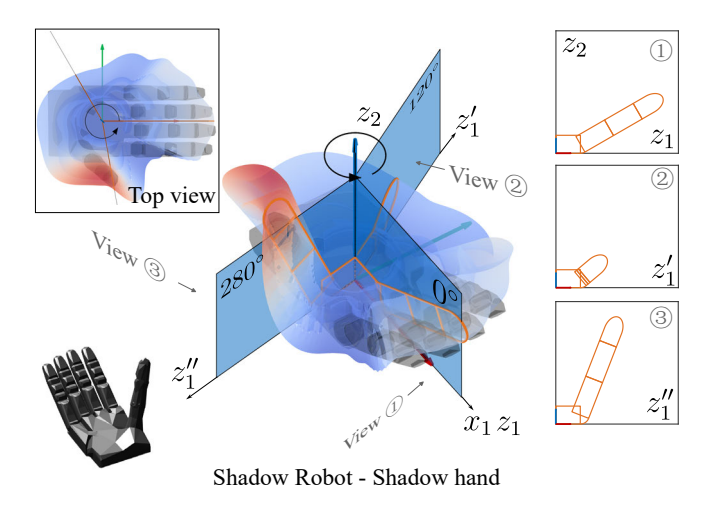


Figure 6: Hand hull $\mathcal D$ for the Shadow hand with three featured rotated planes.

Definition 1. The *hand hull* \mathcal{D} is a surface of revolution [48], generated by rotating a limited number of 2D primitive shapes (e.g., rectangles, ellipses, and sectors), arranged in a single serial tree structure on a half-plane around a hand-fixed axis, with the angle $\alpha = [0, 2\pi)$, cf. Figure 5. The formed interior (i.e., a solid of revolution) is denoted as \mathcal{D}^f . The points on the surface of the revolution are denoted as \mathcal{D}^b , refer to set definitions in Table A.8.

The 3D hand hull integrates the kinematic information of multiple fingers into a single tree structure. In this representation, each finger segment, including the palm, is approximated by the center positions and orientations of 2D primitive shapes on this tree, which encode the real finger joint's configuration and the rotation angle α , which defines the plane intersecting the physical fingers, see Section Appendix A.3 for details. By designing a rotation-angle (α) dependent length for every 2D primitive shape, the resulting hand hull encompasses regions such as the hypothenar eminence or the interdigital areas and forms a 3D continuous entity around the hand-fixed axis, refer Section Appendix A.2 for more details.

Importantly, the estimation of finger joint positions and segment lengths is not limited to specific types of hand or finger kinematics. This hull is adaptable to different hand types and dynamically updated according to feedback on finger joint configurations, e.g., a hand hull for a Shadow hand is depicted in Figure 6. In certain finger joint configurations, such as performing a power grasp, the hull may not fully encompass all the fingers, as demonstrated in the closed-hand mesh shown in Figure 11 (d). This intentional design avoids creating a self-intersecting mesh (cf. Figure 4 (d)) during power grasping and allows the guiding motion to persist while the fingers continue closing.

4. Hand Motion Generation

This section presents a guiding flow design for generating a hand-reaching motion. We begin by formulating the reaching-motion generation problem in Section 4.1 as the design of two

dynamical systems to achieve the desired pose determined by grasp generation or synthesis. In Section 4.2, we introduce a semi-tangent flow, which generates an reaching motion for the object with a given hand hull (see Definition 1). The guiding motion for the hand is achieved by reversing the semi-tangent flow and incorporating an orientation regulator, as detailed in Section 4.3. Finally, in Section 4.4, we provide a formal proof of convergence and collision avoidance for static unperturbed spherical objects. In this section, we will not consider the effect of the finger's movement during arm reaching.

4.1. Problem Statement

We view the generation of approaching motion as the design of two separate dynamical systems: one governing translational movement and the other regulating rotational movement.

Translational Motion:. Let $\mathbf{x} = (x_1, x_2, x_3) \in \Omega \subset \mathbb{R}^3$ be the position of an object's Geometric Center (GC), denoted as P in a hand-fixed frame $\{\mathcal{H}\}$. The set $\Omega := B(\mathbf{x}^*, c)$ is a bounded ball containing the desired object's GC location \mathbf{x}^* (denoted as P_d), given by the grasp generation, where the radius $0 < c < \infty$. We seek a first-order autonomous dynamical system describing the temporal evolution of P

$$\dot{\mathbf{x}} = \mathbf{f}_t(\mathbf{x}),\tag{1}$$

where $f_t: \Omega \to \mathbb{R}^3$ holding following objectives:

- (O1) Convergence: The object x converges to the attractor x^* , i.e., $||x x^*|| \to 0$ as $t \to \infty$.
- (O2) **Collision-free**: As $x \to x^*$, x must not penetrate the hand hull \mathcal{D} (see Definition 1), guaranteeing the object never collides with the fingers during the approach.

Rotational Motion:. Let ${}^{\mathcal{H}}\mathbf{R}_o \in SO(3)$ be the orientation of an object-fixed frame described in the hand frame $\{\mathcal{H}\}$. Our objective is to design a dynamical system

$$\omega = f_r(^{\mathcal{H}} \mathbf{R}_o), \tag{2}$$

where $f_r: SO(3) \mapsto \mathbb{R}^3$ to achieve the desired orientation ${}^{\mathcal{H}}\mathbf{R}_{o,d} \in SO(3)$, given by grasp generation. The design of the translational dynamical system is introduced in Section 4.2, and for regulating orientation motion in Section 4.3.

4.2. Semi-tangent Flow: An Attractive and Collision-Avoiding Translational Velocity Field for Object

We introduce a semi-tangent flow that employs the hand hull \mathcal{D} as a representation of obstacles to generate a translational velocity reference for the object. This reference guides the object toward the desired location P_d while ensuring no finger-object collision. The proposed approach achieves this by integrating a globally attractive linear field with a locally collision-avoiding tangent flow.

Given that the hand hull \mathcal{D} is constructed by rotating a 2D kinematic tree around a fixed axis, the design of a 3D collision-avoiding dynamical system can be effectively reduced to the design of a 2D dynamical system on each rotated plane. This reduction is applicable when the object is situated above the dorsal plane (refer to the light grey plane in Figure 7 (e)).

Guiding axis

For scenarios where the object is located beneath the dorsal plane, it is necessary to define a guiding axis (as pictured in Figure 7 (g)). This axis specifies an intended guiding direction, ensuring that the object is maneuvered around the fingers in accordance with the user's intent (e.g., side approach of the object), as exemplified in Figure 7 (h).

Remark 2. For an example of fast reaching of a tabletop cylindrical object scenario, we believe the approaching and grasping from the side typically yields higher success rates than a top-down approach because the side approach requires less precise timing for finger closure and, similar to caging grasps, is more robust against the object pose uncertainties from the visual tracking.

Consequently, the formulation requires addressing two distinct cases: when the object is positioned on the palmar side and when it is located on the dorsal side.

Thus, prior to formally distinguishing and addressing these two cases, we first establish the hand-fixed coordinate system $\{\mathcal{H}\}$, see Figure 8 (a). The x_1x_2 -plane is defined by the dorsal plane. The axis x_3 , which represents the rotational symmetry axis of the hand hull \mathcal{D} , is oriented such that its positive direction extends away from the palm. The origin O is located at the intersection of the x_3 -axis with the dorsal plane (x_1x_2 -plane). Furthermore, the positive x_1 -axis is the guiding axis that lies within the dorsal plane, passes through the origin, and points toward the middle fingertip. This x_1 is user-defined. As shown in Figure 7 (g), one of the directions satisfying our desired approaching strategy is illustrated in Figure 2.

4.2.1. Object on Palmar Side $x_3 \ge 0$

When the object is located above the palm, we define a dynamic plane as follows:

Definition 2 (*Dynamic plane*). Let r be a vector originating at the origin O of $\{\mathcal{H}\}$ and pointing toward the object's CoM position x. The plane spanned by r and the x_3 -axis is called the *Dynamic plane* (DP), see the blue plane in Figure 8 (a). The angle between DP and the x_1x_3 -plane is denoted as α .

Remark 3. The DP becomes undefined when r is parallel to the x_3 -axis, which occurs when the object is positioned on the hand-fixed axis. This specific scenario will be addressed when designing the final dynamical system.

Remark 4. When the DP intersects the spherical object through its GC, it forms a circle with radius r_0 on the dynamic plane. Additionally, this intersection produces a cross section of the hand hull \mathcal{D} , which corresponds the rotated 2D plane with angle α used in constructing the 3D hand hull.

We use the planar coordinate z to represent the position of the object's GC, as visualized in Figure 8 (a). The coordinate is expressed as $z = \operatorname{col} \begin{bmatrix} z_1 & z_2 \end{bmatrix} \in \Omega_z$, where $\Omega_z = B(z^\star, c_z) \subset \mathbb{R}^2$ and $0 < c_z < \infty$. We illustrate the planar semi-tangent flow design on each dynamic plane in three steps.

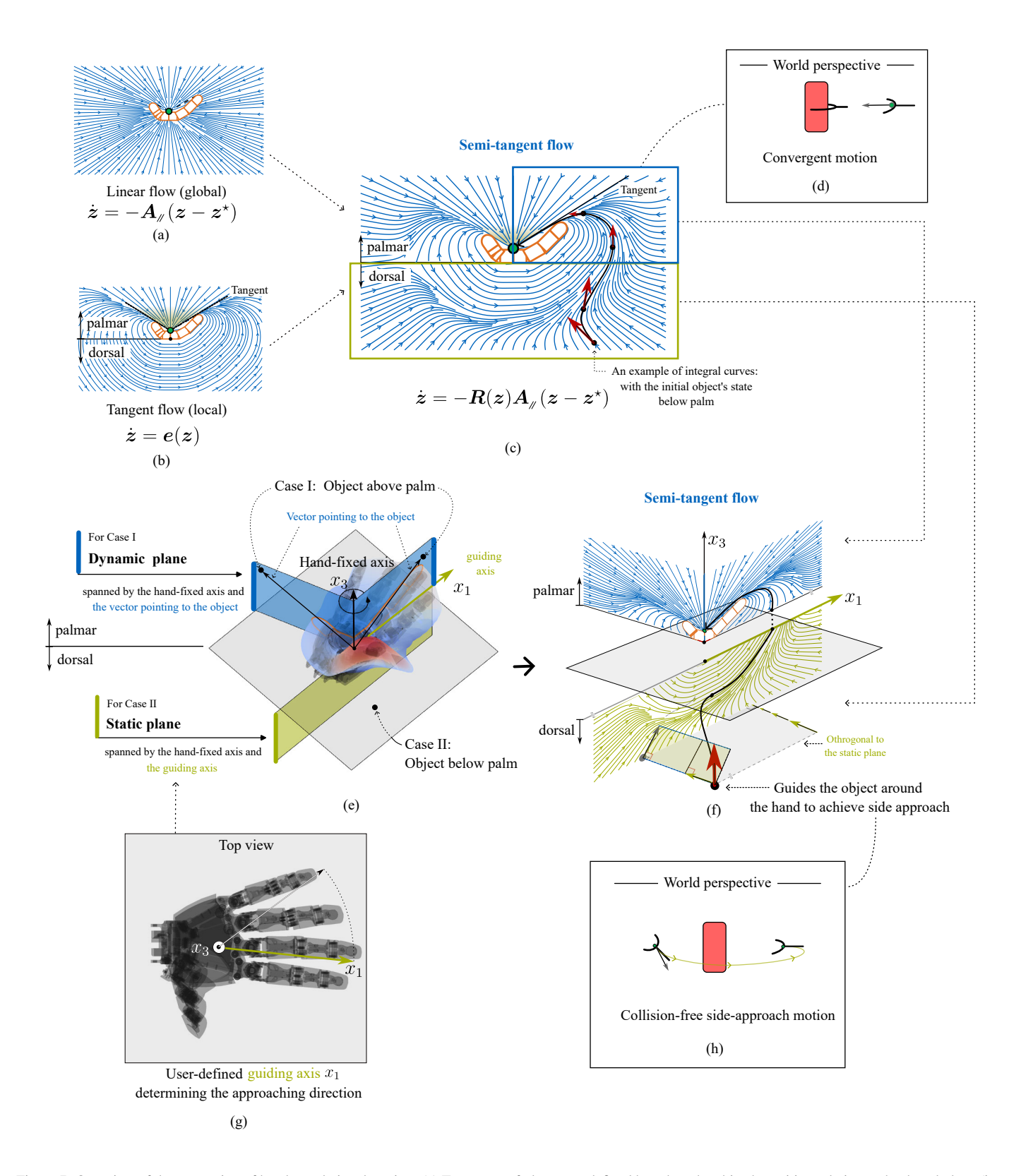
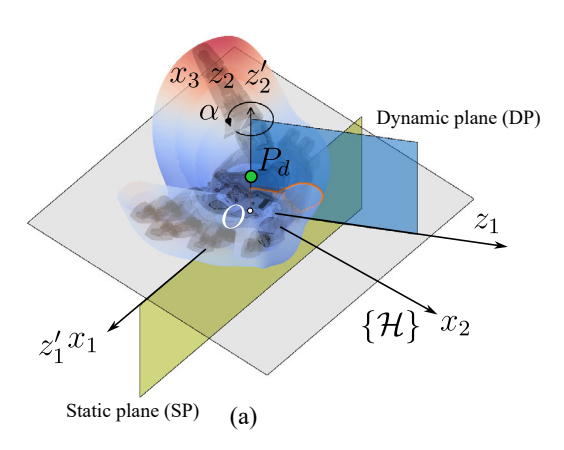


Figure 7: Overview of the generation of hand translational motion. (e) Two types of planes are defined based on the object's position relative to the dorsal plane (in light grey), differentiating the palmar and dorsal sides of the hand. Specifically, the dynamic plane is spanned by the hand-fixed axis and a vector passing through the current object's geometric center, while the static plane is fixed to the hand and spanned by the guiding axis i.e., a user-defined approaching direction (g) and the hand-fixed axis. The semi-tangent flow (c) is designed within these two types of planes, combining a global linear flow (a) that attracts the object and a tangent flow (b) that guides the object along the hand hull. The spatial representation of the semi-tangent flow is shown in (f). For objects on the palmar side, the dynamic plane induces a convergent motion (d). Conversely, for objects positioned below the palm, when the static plane does not consistently intersect with the object, an additional orthogonal flow draws the object toward the plane. This results in a collision-free side-approach motion from the world frame perspective (h). Finally, the guiding motion command for the hand is derived by reversing the semi-tangent flow.



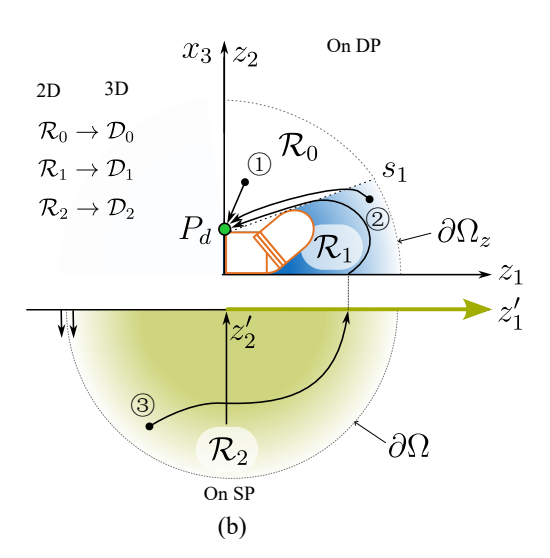


Figure 8: (a) The definition of the hand-fixed coordinate system $\{\mathcal{H}\}$ with two types of planes. (b): Since the hand hull is generated by a 2π -rotation of a plane around the hand-fixed axis, we only depict half of the dynamic plane (DP) for clarity. The relevant regions on the DP are as follows: \mathcal{R}_0 , whose solid of revolution forms \mathcal{D}_0 , and \mathcal{R}_1 , which represents the exterior region outside the hand hull. The solid of revolution corresponding to \mathcal{R}_1 is denoted as \mathcal{D}_1 . Three examples of integral curves are shown for initial object locations marked as $\widehat{1}$, $\widehat{2}$, and $\widehat{3}$.

As the first step, we design a global linear attractive flow on the plane, i.e.,

$$\dot{z} = f_{t,w}(z) = -A_{\mathscr{I}}\tilde{z} = -\begin{bmatrix} a_1\tilde{z}_1 \\ a_3\tilde{z}_2 \end{bmatrix}, \tag{3}$$

where the error is defined as $\tilde{z} = z - z^*$, and the attractor P_d is positioned on the hand-fixed axis, i.e., $z^* = \text{col}\left[0, z_2^*\right]$. The positive diagonal matrix in Eq. (3) is given by

$$A_{/\!/} = \text{diag}(a_1, a_3) > 0, \quad \text{with } a_1 \ge a_3.$$
 (4)

This design ensures that the convergence in the z_2 direction is slower or equal to the convergence in the other two. This property is later required for the proof of Lemma 2.

We proceed by defining a region on the dynamic plane, denoted as \mathcal{R}_0 , as shown in Figure 8 (b). The region \mathcal{R}_0 is constructed as follows: Consider a line parallel to the z_2 -axis that passes through the attractor point P_d (indicated by the green dot). This line is rotated clockwise about P_d until it first touches the hand hull. We refer to this line as s_1 (refer Eq. (B.12) for definitions). The area between the z_2 -axis, s_1 and an upper bound $\partial\Omega_z$ (including all boundaries) is defined as \mathcal{R}_0 Eq. (A.16). Furthermore, the region enclosed by s_1 and the s_1 -axis, which lies outside the hand hull s_2 , is denoted as s_3 , and the region below the palm is denoted as s_3 refer to the set definition in Table A.8. Since collisions between the fingers and the object are anticipated to occur within s_3 during grasping, the linear flow given by Eq. (3) remains unaltered in s_3 0.

As a second step, we introduce the *tangent flow*, denoted as $e(z) \in \mathbb{R}^2$, depicted in Figure 7 (b). This flow is defined exclusively for points z within the region \mathcal{R}_1 . It represents a unit vector tangent to the hand hull \mathcal{D} , providing the local direction of motion. The closed-form expressions for this flow are given in Eq. (B.1) and detailed in Section Appendix B. Additionally, the tangent flow is designed to ensure consistency and continuity when z crosses s_1 . This behavior is demonstrated by an example integral curve originating from the initial object location (2) in Figure 8 (b) and further elaborated in Section Appendix B.3.

As the third step, we generate a semi-tangent flow, which is locally tangent to hand hull Figure 7 (b) and globally linear as shown in Figure 7 (a), the final flow is shown in Figure 7 (c). This is achieved by locally rotating the linear flow $f_{t,w}$ Eq. (3) in the neighborhood of the hand hull through a rotation matrix $R(\gamma(z))^2$, where the angle $\gamma(z) \in (-\pi, \pi)$ depends on the distance. This ensures a seamless transition between the tangent and linear flows. The resulting semi-tangent flow is described by

$$\underbrace{\begin{bmatrix} \dot{z}_1 \\ \dot{z}_2 \end{bmatrix}}_{\dot{z}} = \underbrace{-\begin{bmatrix} \cos(\gamma(z_1, z_2))a_1\tilde{z}_1 + \sin(\gamma(z_1, z_2))a_3\tilde{z}_2 \\ -\sin(\gamma(z_1, z_2))a_1\tilde{z}_1 + \cos(\gamma(z_1, z_2))a_3\tilde{z}_2 \end{bmatrix}}_{\mathbf{R}^{\mathsf{T}}(\gamma(z))f_{t,w} = -\mathbf{R}^{\mathsf{T}}(\gamma(z))A_{\mathscr{I}}\tilde{z}}, \tag{5}$$

$${}^{2}\mathbf{R}(\gamma) = \begin{bmatrix} \cos \gamma & -\sin \gamma \\ \sin \gamma & \cos \gamma \end{bmatrix} \in SO(2)$$

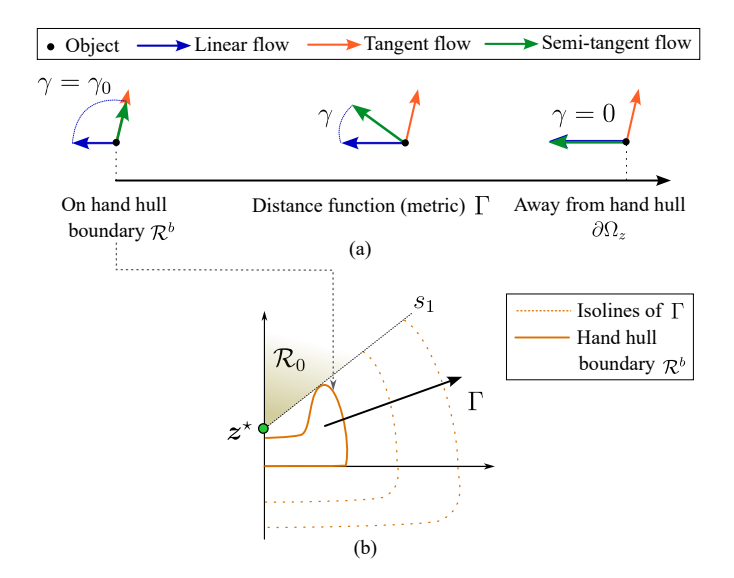


Figure 9: (a): Illustration of the angle $\gamma(\Gamma)$, which partially rotates the linear flow to the direction of the tangent flow, depending on the distance function Γ . (b): The isolines of the distance function (metric) $\Gamma(z)$ in the neighborhood of the hand hull. Note that the metric is undefined within \mathcal{R}_0 , as no rotation is defined in this region.

where $\gamma(z)$ is defined by

$$\gamma(z) = \eta(\Gamma(z)) \cdot \gamma_0(z), \tag{6}$$

where $\Gamma(z)$ is a smooth distance function characterizing the distance between a point z and the finger segment center defined in Eq. (B.15), see Figure 9 (a) and (b). The $\eta(\cdot) \in [0,1]$ is a smooth distance-dependent transition function that can be customized by the user. An example design for $\eta(z)$ is provided in Eq. (B.14), with further details in Section Appendix B.4.

The $\gamma_0(z)$ in Eq. (6) parameterizes the rotation angle between the linear flow $f_{t,w}$ Eq. (3) and tangent flow e Eq. (B.1) at the same location z, written as

$$\gamma_0(z) := \operatorname{sgn}(f_{t,w}(z) \wedge e(z)) \operatorname{arccos} \frac{f_{t,w}(z)^{\top} e(z)}{\|f_{t,w}(z)\|}, \tag{7}$$

where the exterior product (or wedge product) is denoted as " \wedge ", which generalizes the cross product definition " \times ". $||f_{t,w}(z)|| \neq 0$ is valid for all $z \in \mathcal{R}_1$. In short, the resulting semi-tangent flow Eq. (5) has the following features:

- When the object z is located on the boundary of the hand hull $\forall z \in \mathcal{R}^b$, the semi-tangent flow aligns with the tangent flow but retains the magnitude of the linear flow, i.e., $\dot{z} = e(z) \cdot ||f_{t,w}(z)||$, and with the rotation angle satisfies $\gamma(z) = \gamma_0(z)$, see the left plot of Figure 9 (a).
- When the object moves away from the boundary of the hand hull, the semi-tangent flow transitions to the linear attractive flow. i.e., $\gamma(z) = 0$, as $z \to \partial \Omega_z$, see the right plot of Figure 9 (a).

Finally, the dynamical system on the palmar side can be expressed as $g: \Omega_z \mapsto \mathbb{R}^2$:

$$\dot{z} = g(z) = \begin{cases} Eq. (3) & z \in \mathcal{R}_0 \\ Eq. (5) & z \in \mathcal{R}_1 \end{cases}$$
 (8)

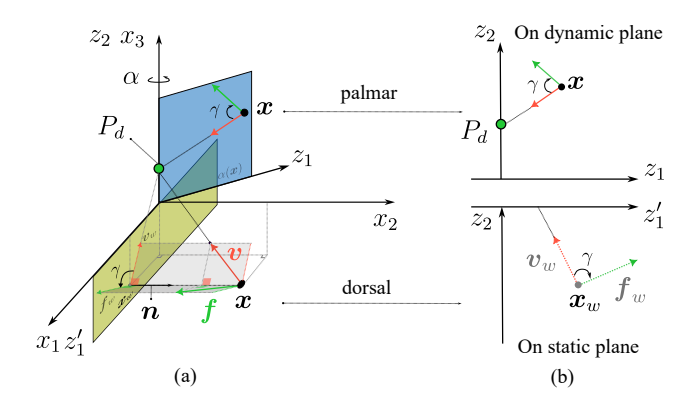


Figure 10: The geometric interpretation of 3D semi-tangent flows, which is a result from the rotation of a global linear attractive flow ν around normal vector n(x) of DP or SP with the rotation angle γ .

Remark 5. Notably, by design, the tangent flow e(z) aligns with the direction of the linear flow Eq. (3) when z lies on the tangent s_1 . Consequently, the resulting Eq. (5) becomes equivalent to Eq. (3) for all $z \in s_1$, where $s_1 \subset \mathcal{R}_0$. Therefore, we can conclude that Eq. (8) is continuous for all $z \in \mathcal{R}_0 \cup \mathcal{R}_1$.

4.2.2. Object on Dorsal Side $x_3 < 0$

Definition 3 (*Static plane*). The hand-fixed *Static plane* (SP) is spanned by the x_1 - and x_3 -axes, see the green plane in Figure 8 (a).

We design a global attractive linear dynamical system

$$\dot{x} = -A\tilde{x}, \quad \tilde{x} = x - x^*, \tag{9}$$

where the attractor x^* is the defined in Eq. (3) rewritten in the spatial coordinate $x^* = (0, 0, x_3^*)$, where $x_3^* = z_2^*$. The positive diagonal matrix A is defined by

$$A = diag(a_1, a_1, a_3) > 0.$$
 (10)

The object's position x on the dorsal side does not always reside within the static plane. In such cases, we only rotate the component of the linear flow Eq. (9) parallel to x_1x_3 -plane, and the orthogonal component (along the x_2 -axis) remains unaffected. The rotation $\gamma(x_1, x_3)$ of the velocity component within the x_1x_3 -plane around the x_2 -axis adheres to the same design outlined in Eq. (6). The arguments of $\gamma(x_1, x_3)$ are derived from the mapping $z_1 = x_1$ and $z_2 = x_3$.

The dynamical system with the designed semi-tangent flow $f: \Omega \mapsto \mathbb{R}^3$ is given by

$$\begin{bmatrix}
\dot{x}_1 \\
\dot{x}_2 \\
\dot{x}_3
\end{bmatrix} = - \begin{bmatrix}
\cos(\gamma(x_1, x_3))a_1\tilde{x}_1 + \sin(\gamma(x_1, x_3))a_3\tilde{x}_3 \\
a_1\tilde{x}_2 \\
-\sin(\gamma(x_1, x_3))a_1\tilde{x}_1 + \cos(\gamma(x_1, x_3))a_3\tilde{x}_3
\end{bmatrix}, (11)$$

where $R_n(\gamma)^3$ represents the rotation around the normal vector n of the SP

$$\mathbf{n} = \operatorname{col} \begin{bmatrix} 0 & 1 & 0 \end{bmatrix}, \tag{13}$$

³It is computed with the *Rodrigues*' rotation formula by giving angle-axis

with the rotation angle $\gamma(x)$ Eq. (6). This process is visualized on the dorsal side of the hand in Figure 10 (a): rotate the linear vector (\mathbf{v} in red) around the normal vector (\mathbf{n} in black) of the static plane (x_1x_3 -plane in green), then get the semi-tangent flow (\mathbf{f} in light green). Notably, when the object's initial position is below the dorsal plane, the integral curve of the semi-tangent flow will eventually reach the plane $z_2 = 0$ (or equivalently $x_3 = 0$), as depicted in Figure 7 (f). Figure 11 visualizes the semi-tangent flow in the whole space for two configurations of the finger joints.

4.3. Guiding Flow for Hand

This section presents the designed dynamical systems achieving Eq. (1) and Eq. (2) in our defined problem statement and presents the guiding velocity reference for the hand.

We first map the object location from x to z for the object on the palmar side, given by

$$\underbrace{\begin{bmatrix} z_1 \\ z_2 \end{bmatrix}}_{z} = \underbrace{\begin{bmatrix} \cos \alpha & \sin \alpha & 0 \\ 0 & 0 & 1 \end{bmatrix}}_{N} \underbrace{\begin{bmatrix} x_1 \\ x_2 \\ x_3 \end{bmatrix}}_{x}, \tag{14}$$

where the rotation angle is computed by $\alpha = \text{mod}(\text{atan2}(x_2, x_1), 2\pi)^4$, for all $\mathbf{x} \in \mathcal{D}_1 \cup \mathcal{D}_0 \setminus \mathcal{D}_a$. The set \mathcal{D}_a represents when the object's is located on the x_3 -axis and above the attractor \mathbf{x}^* , defined by

$$\mathcal{D}_a = \{ \mathbf{x} \in \Omega \mid x_1 = 0, x_2 = 0, x_3 \ge x_3^* \}. \tag{15}$$

This set is defined mainly to exclude the case of undefined DPs mentioned in Remark 3. Using Eq. (14) to relate the z- and x-spaces, we can embed the 2D z-dynamics into the 3D x-space, yielding a unified expression for the overall dynamics in a consistent coordinate system. Notably, no dynamics is specified in the third independent dimension, which is represented by the rotation angle α in Eq. (14), as it complements the z_1 and z_2 coordinates. This is because the object z on the palmar side stays always within a DP, as defined in Definition 2. Consequently, $\dot{\alpha}=0$. Since $NN^{\top}=I_{2\times 2}$, $\dot{\alpha}=0$ and using Eq. (3), Eq. (5), and Eq. (14), we differentiate both sides of Eq. (14) w.r.t. time, and re-arrange terms to derive

$$\dot{x} = -\underbrace{N^{\top} R^{\top} (\gamma(Nx)) A_{/\!/} N}_{S(x)} \tilde{x}. \tag{16}$$

representation (angle, axis)= $(\gamma(x), n)$, written as

$$\mathbf{R}_{\mathbf{n}}(\gamma) = \mathbf{I}_{3\times 3} + \sin \gamma [\mathbf{n}]_{\times} + (1 - \cos \gamma) [\mathbf{n}]_{\times}^{2}, \tag{12}$$

where the operator []x is defined by

$$[\mathbf{n}]_{\times} = \begin{bmatrix} 0 & -n_3 & n_2 \\ n_3 & 0 & -n_1 \\ -n_2 & n_1 & 0 \end{bmatrix}.$$

⁴The function $\operatorname{atan2}(y, x)$ is the four quadrant arctangent of the coordinate of x and y such that $\operatorname{atan2}(y, x) \in [-\pi, \pi)$. The function $\operatorname{mod}(\cdot, 2\pi)$ computes the modulus after division, which turns the results in the interval $[0, 2\pi)$.

Therefore, using Eq. (16), the dynamical system Eq. (8) on the palmar side is expressed in x-space as

$$\dot{\mathbf{x}} = \begin{cases} -\operatorname{col} \begin{bmatrix} 0 & 0 & a_3(x_3 - x_3^{\star}) \end{bmatrix} & \mathbf{x} \in \mathcal{D}_a \\ -\mathbf{S}(\mathbf{x})\tilde{\mathbf{x}} & \mathbf{x} \in \mathcal{D}_0 \cup \mathcal{D}_1 \setminus \mathcal{D}_a. \end{cases}$$
(17)

Combining Eq. (17) and Eq. (11) leads to the final definition of semi-tangent flow:

Definition 4 (*Semi-tangent flow*). The semi-tangent flow f_t : $\Omega \mapsto \mathbb{R}^3$ for every given object's GC location x, is given as

$$\dot{\mathbf{x}} = \mathbf{f}_{t}(\mathbf{x}) = \begin{cases} -A\tilde{\mathbf{x}} & \mathbf{x} \in \mathcal{D}_{a} \\ -S(\mathbf{x})\tilde{\mathbf{x}} & \mathbf{x} \in \mathcal{D}_{0} \cup \mathcal{D}_{1} \setminus \mathcal{D}_{a} \\ -\mathbf{R}_{n}(\gamma(\mathbf{x}))A\tilde{\mathbf{x}} & \text{otherwise} \end{cases}$$
(18)

where the positive matrix A is given in Eq. (10), S(x) in Eq. (16), the rotation matrix $R_n(\cdot)$ in Eq. (12), the normal vector n in Eq. (13), and the rotation angle $\gamma(x)$ in Eq. (6).

4.3.1. Velocity Reversal

It has been assumed that the object is actively actuated, while the fingers and palm remain passively fixed in a static reference frame. To compute the final body velocity reference for the hand, the designed velocity is set as the negative of the object's reference velocity, as expressed in

$$\mathbf{v}_r = -\mathbf{f}_t(\mathbf{x}). \tag{19}$$

4.3.2. Orientation Regulator

The orientation regulation is designed to achieve significantly faster convergence compared to the translational dynamic system. This can be accomplished by utilizing rapid convergence motions for lower-inertia links on the arm, such as underarm rotation. This fast convergence in orientation ensures that the assumption for a circular cross-section remains valid not only for spherical objects but also for cylindrical ones. Based on this, we design our rotational dynamical system Eq. (2) using a spring-like potential field, as introduced in [49, 50]

$$\omega_r = \operatorname{asym}(^{\mathcal{H}} \mathbf{R}_{o,d} \mathbf{G}), \tag{20}$$

where the asymmetric part of a matrix (\cdot) is defined as $\operatorname{asym}(\cdot) = \frac{1}{2}((\cdot) - (\cdot)^T)$. The orientation error ${}^{\mathcal{H}} R_{o,d}{}^5$ is calculated by the desired object pose in the hand frame. The co-stiffness matrix $G = \frac{1}{2}\operatorname{tr}(K)I - K \in \mathbb{R}^{3\times 3}$ with $K = \operatorname{diag}(k_1, k_2, k_3) > 0$ generates the angular velocity to the desired orientation. By stacking Eq. (19) and Eq. (20), we obtain the body velocity reference for the object

$$\chi_r = \begin{bmatrix} v_r \\ \omega_r \end{bmatrix}. \tag{21}$$

$$^{\mathcal{H}}\mathbf{R}_{o,d} = {^{\mathcal{W}}\mathbf{R}_{\mathcal{H}}^T}{^{\mathcal{W}}\mathbf{R}_O}{^{\mathcal{O}}\mathbf{R}_{o,d}} = {^{\mathcal{H}}\mathbf{R}_O}{^{\mathcal{O}}\mathbf{R}_{o,d}},$$

where \mathcal{W} and O represent the world frame and the object-fixed frame, respectively. Here, ${}^OR_{o,d}$ denotes a more commonly desired grasp pose expressed in the object frame given by the grasp generator, while the live object pose feedback HR_O is obtained through vision-based tracking.

⁵Through hand-eye calibration, the desired object frame relative to the hand frame is determined using the following relation:

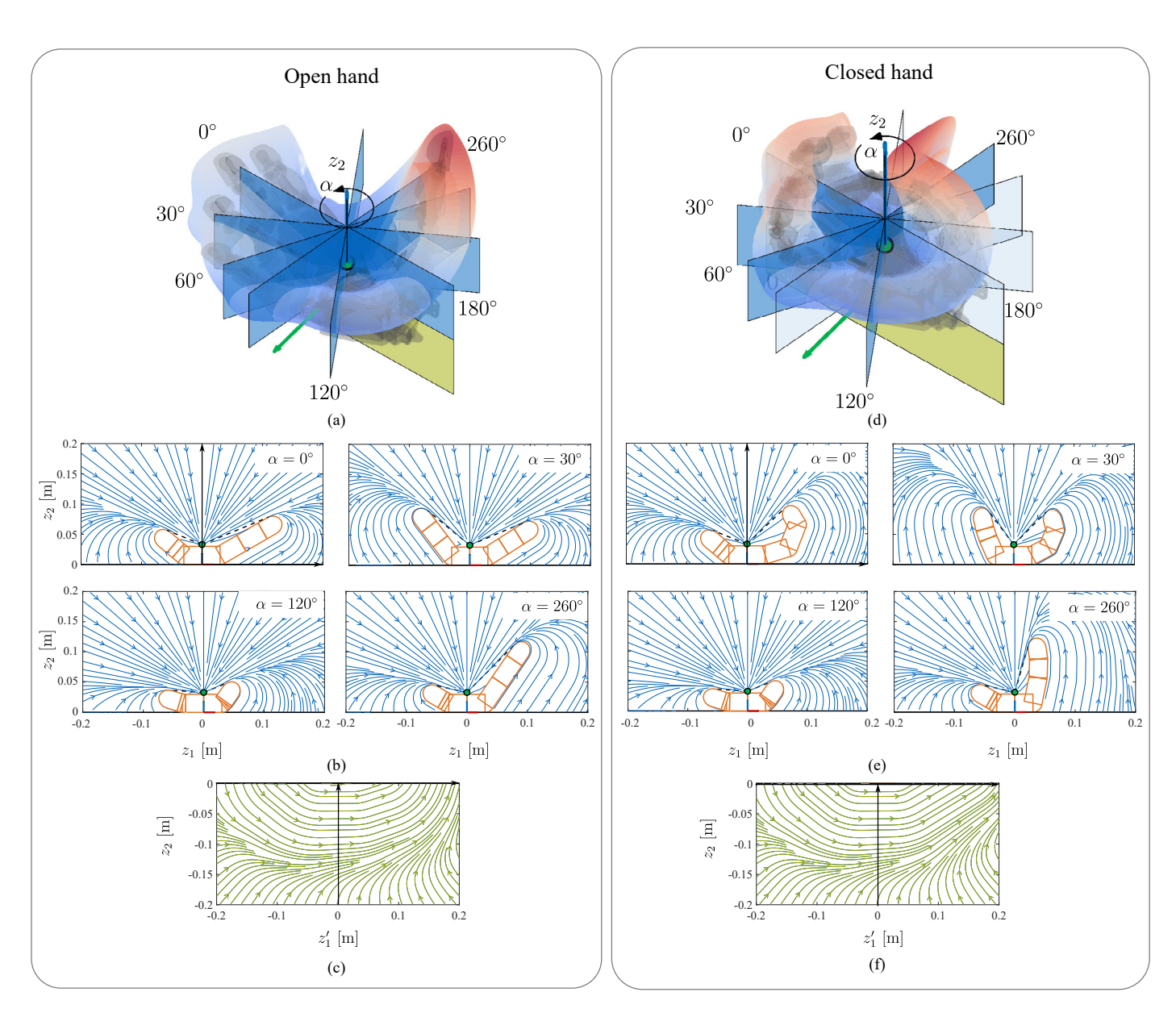


Figure 11: Semi-tangent flow in two finger configurations: open hand (a) and closed hand (b). The left (a-c) and right columns (d-f) depict (b) the hand hull \mathcal{D} with dynamic planes (see (b) and (e) in blue) and rotated angles α , and static planes (see (c) and (f) in green). The streamlines represent the integral curves of the designed vector field on each plane.

Note that the current design assumes the instantaneous relative velocity between the object and the hand to be zero. If the actual object's velocity denoted as χ_o , is measurable or predictable, the guiding flow for the hand—represented by the body velocity reference in Eq. (21)—is added by χ_o . The updated hand velocity reference is computed as $\chi_r + \chi_o$, where the first term, χ_r , generates the attractive and collision-avoiding motion between the object and the hand, and the second term, χ_o , ensures synchronization of the hand motion with the actual object velocity. This latter term is governed by the object dynamics or other external forces influencing χ_o .

Remark 6. The velocity synchronization will not change the relative object pose to the hand. In practice, the object's velocity estimation of χ_o is challenging due to the limited tracker's refreshing rate, which causes less-satisfied numeric differentiation of the pose, especially when the object is not predictable, e.g., the object being co-grasped by a human, and handed over to the robot, or the object being attached to a constantly disturbed string, or unexpected disturbance. Therefore, we assume $\chi_o = \mathbf{0}$ and utilize χ_r Eq. (21) as final references in the following experimental validation section.

As a summary of this section, a pseudo-code is presented in Algorithm 1.

4.3.3. Joint Velocity Reference:

The generated body velocity χ_r Eq. (21) is mapped via the body Jacobian $J \in \mathbb{R}^{6 \times n}$ w.r.t. the hand frame $\{\mathcal{H}\}$ to the joint velocity reference $\dot{q}_{a,r}$ in Figure 3, which is expressed as

$$\dot{\boldsymbol{q}}_{a,r} = \boldsymbol{J}^{\sharp} \boldsymbol{\chi}_r + (\boldsymbol{I} - \boldsymbol{J}^{\sharp} \boldsymbol{J}) \, \dot{\boldsymbol{q}}_{\text{null}}, \tag{22}$$

where the last term includes a right-hand Moore-Penrose pseudoinverse $J^{\#} = J^{\top}(JJ^{\top})^{-1}$, and $\dot{q}_{\text{null}} \in \mathbb{R}^n$ the nullspace reference velocity. The design of nullspace velocities is out of the scope of this work.

4.4. Convergence and Collision Avoidance

We prove that the dynamical systems in Eq. (8) and Eq. (11) achieve the objectives (O1) and (O2), defined in Section 4.1. As stated in the objectives, only the translational dynamics is considered.

4.4.1. Uniqueness of Integral Curves

Lemma 1. Consider the autonomous dynamic systems defined by Eq. (8) and Eq. (11). A unique integral curve x(t) (or: z(t)) exists with a unique bounded initial state $x(0) \in \Omega$ (or: $z(0) \in \Omega_z$).

Proof. The proof follows the example in [51, pp. 388], summarized in two steps:

- 1) Prove that f in Eq. (11) and g in Eq. (8) are Lipschitz continuous.
- 2) Prove the existence of a unique trajectory x(t) of the dynamical system with a unique bounded initial state $x(0) \in \Omega$ in the sense of Filipov [52, 53, 51].

Algorithm 1 Hand Motion Generation

Input: Current object state in the hand-fixed frame $({}^{\mathcal{H}}\mathbf{R}_{O}, \mathbf{x})$, desired grasp pose $({}^{\mathcal{H}}\mathbf{R}_{O,d}, \mathbf{x}^{\star})$, current finger joint position \mathbf{q}_{f} .

```
Output: Body velocity reference for the hand \chi_r.
  1: while {A stable grasp is not yet confirmed.} do
            \mathcal{D} \leftarrow \{ \text{update hand hull with } \boldsymbol{q}_f \}.
  2:
            f_t \leftarrow \text{Eq. (9)} {update the global attractive linear field}.
  3:
            if x \in \mathcal{D}_0 \cup \mathcal{D}_1 \setminus \mathcal{D}_a then
  4:
  5:
                  z \leftarrow \text{Eq. } (14) \{ \text{map } x \text{ to } z \}.
  6:
                  e \leftarrow \text{Eq.}(B.1) {calculate the tangent flow}.
  7:
                  \gamma \leftarrow \text{Eq. (6)} \{ \text{compute the rotation angle} \}.
  8:
                  f_t \leftarrow \text{Eq.} (16).
            else if x \in \mathcal{D}_a then
  9:
                  f_t \leftarrow \text{Eq. } (9) \text{ {keep the linear flow }}.
 10:
11:
12:
                  f_t \leftarrow \text{Eq.}(11).
13:
14:
            v_r \leftarrow \text{Eq.} (19) {reverse the velocity for the hand}.
15:
            \omega_r \leftarrow \text{Eq. (20)} {get angular velocity reference}.
16:
            \chi_r \leftarrow \text{Eq. (21)} \{ \text{get body velocity reference} \}.
17: end while
```

Step 1: We consider two states x, x' within the same region, e.g., x and x' both in \mathcal{D}_2 . It is sufficient to show that

$$||f(x) - f(x')|| \le L||x - x'||.$$
 (23)

We expand the left side of Eq. (23) using

$$||f(x) - f(x')|| = ||R_n(\gamma(x))A\tilde{x} - R_n(\gamma(x'))A\tilde{x}'||.$$
 (24)

By using the triangle inequality, we have

$$||f(x) - f(x')|| \le ||R_n(\gamma(x))A\tilde{x} - R_n(\gamma(x'))A\tilde{x}|| + ||R_n(\gamma(x'))A(x - x')||,$$
(25)

The rotation angle $\gamma(x)$ Eq. (6) is Lipschitz continuous, which is proven in Lemma 3. Hence, there exists a positive value L_{γ} such that

$$|\gamma(x) - \gamma(x')| \le L_{\gamma} ||x - x'||.$$
 (26)

By applying the mean value theorem for matrix functions [54, Theorem5.9] and considering the presence of trigonometric functions in the entries of the rotation matrixEq. (12), we conclude that there exists a constant $L_R > 0$ such that

$$||\mathbf{R}_{n}(\gamma(\mathbf{x})) - \mathbf{R}_{n}(\gamma(\mathbf{x}'))|| \le L_{R}|\gamma(\mathbf{x}) - \gamma(\mathbf{x}')|. \tag{27}$$

Due to $x \in B(x^*, c)$, the error is bounded $\|\tilde{x}\| = \|x - x^*\| \le c < \infty$, and we have $\|A\tilde{x}\| \le c\|A\|$. Using Eq. (26), Eq. (27) and the sub-multiplication of the matrix norm, we have

$$||[R_n(\gamma(x) - R_n(\gamma(x'))]A\tilde{x}|| \le 2cL_{\gamma}L_R||A||||x - x'||.$$
 (28)

The second term of RHS of Eq. (25) is bounded by

$$||R_n(\gamma(x'))A(x-x')|| \le ||A|| ||x-x'||. \tag{29}$$

By substituting Eq. (28) Eq. (29) into Eq. (25), we finally get Eq. (23) with the Lipschitz constant L being

$$L = (2cL_{\gamma}L_R + 1)||A|| = (2cL_{\gamma}L_R + 1)a_1.$$
 (30)

The same procedure can also be applied for proving the Lipschitz continuity of g(z), for all $z \in \mathcal{R}_0 \cup \mathcal{R}_1$.

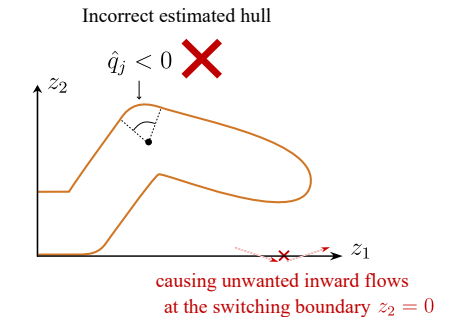


Figure 12: When the estimated finger joint configuration is smaller than the lower bound, this may create a tangent flow that may cross the switching boundary $z_2 = 0$ from the palmar side to the dorsal side.

Step 2: Consider the case when the initial state $x(0) \in \mathcal{D}_2$. Due to the design of the lower-bounded finger joint's configuration $\hat{q}_j > q_{\min}$, see Figure 12 and Section Appendix A.3, we ensure no outward flow and no inward flow [51, Fig 8.7, pp.389] in the neighborhood of the switching plane $x_3 = 0$.

Besides, the inner products of the normal vector \mathbf{n}_{x_3} or (\mathbf{n}_{z_2}) of the switching plane $x_3 = 0$ (or $z_2 = 0$) and velocity vectors before and after crossing the switching boundary $x_3 = 0$, are computed as follows: $\dot{\mathbf{x}}^T \mathbf{n}_{x_3} > 0$ with $x_3 = 0^-$, where $\mathbf{n}_{x_3} = \cot \begin{bmatrix} 0 & 0 & 1 \end{bmatrix}$; and $\dot{\mathbf{z}}^T \mathbf{n}_{z_2} > 0$ with $z_2 = 0^+$ (i.e., $z_3 = 0^+$), where $\mathbf{n}_{z_2} = \cot \begin{bmatrix} 0 & 1 \end{bmatrix}$. Hence, this ensures the flow is consistent before and after crossing the switching boundary, which yields the unique solutions of $\mathbf{x}(t)$ in the sense of *Filipov*. Combining steps 1 and 2 concludes the proof.

4.4.2. Proof of Objective 1 (O1)

The following Lemma 2 is required to show the convergence (in Theorem 1) to the attractor P_d .

Lemma 2. \mathcal{R}_0 is an invariant set according to the Lemma 4.

Theorem 1. Consider the autonomous dynamic systems defined by Eq. (8) and Eq. (11). If $x(0) \in \Omega$, then any trajectory x(t) converges to the attractor x^* (or z^*) as $t \to \infty$.

Proof. The proof discusses three cases (C1 to C3) based on the initial state x(0), marked as (1)-(3) in Figure 8 (b):

- (C1) When the object is initialized on $z(0) \in \mathcal{R}_0$ (see ① in Figure 8 (b)), one must show that z(t) converges to the desired attractor as $t \to \infty$.
- (C2) When $z(0) \in \mathcal{R}_1$ (see ② in Figure 8 (b)), prove z(t) converges to the switching boundary s_1 with a finite time.

(C3) When $\mathbf{x}(0) \in \mathcal{D}_2 : \{\mathbf{x} \in \Omega \mid x_3 < 0\}$ (see ③ in Figure 8 (b)), prove $\mathbf{x}(t)$ converges to the switching plane $x_3 = 0$ (the grey plane in Figure 8 (a)) with a finite time.

By demonstrating that conditions (C1)–(C3) are satisfied, we can conclude that the object will converge to the desired attractor for any initial condition. Specifically, the sets are always traversed in the prescribed order: from \mathcal{D}_2 to \mathcal{R}_1 , and finally to \mathcal{R}_0 . This establishes the required convergence result.

Case (C1): For $z \in \mathcal{R}_0$, the dynamical system is described by Eq. (3). Since $-A_{\mathscr{N}} = -\mathrm{diag}(a_1, a_3)$ is $\mathit{Hurwitz}$ it follows that for any initial state in \mathcal{R}_0 defined in Eq. (A.16), Eq. (3) converges exponentially to the attractor z^{\star} , as $t \to \infty$. Furthermore, the set \mathcal{R}_0 is an invariant set (see Lemma 2), since the rate of convergence in the z_1 direction is always greater than or equal to the rate in the z_2 -direction since $a_1 \ge a_3$.

Case (C2): Firstly, the integral curves of Eq. (5) originating from \mathcal{R}_1 will not cross the switching boundary $x_3 = 0$. This is ensured by the lower-bounded configuration of the finger joint, $\hat{q}_j > q_{\min}$ (see Figure 12), and the design of the rotation angle $\gamma(z)$ in Eq. (6), which collectively guarantee that the vector field Eq. (5) does not cross the switching boundary $x_3 = 0$. Secondly, z(t) converges to the s_1 , due to the design of tangent flow e Eq. (B.1) in Section Appendix B. Thirdly, the vector field of Eq. (5) is lower bounded since $\|\mathbf{R}(\gamma(z))\mathbf{A}_{\mathscr{N}}\cdot(z-z^*)\| \geq a_3x_3^* > 0$. where $\mathbf{A}_{\mathscr{N}}$ is given in Eq. (3). The combination of all three steps ensures that z(t) converges to s_1 within a finite time $t_1 < \infty$ and subsequently enters the invariant set \mathcal{R}_0 . The subsequent proof of convergence to the attractor z^* proceeds in the same way as the proof for Case (C1).

Case (C3): Similar to the approach in Case (C2): the lower-bounded finger joint's configuration $\hat{q}_j > q_{\min}$ and the design of tangential flow near the fingertip guarantee that x(t) according to Eq. (11) converges to the switching plane $x_3 = 0$. Besides, the vector field in Eq. (11) is lower bounded for all $x \in \mathcal{D}_2$ due to $||R_n(\gamma(x))A \cdot (x - x^*)|| \ge a_3 x_3^* > 0$. Therefore, x(t) converges to $x_3 = 0$ with a finite time $t_f < \infty$. x(t) will leave the switching plane $x_3 = 0$ as $t > t_f$ due to the consistent flow at $x_3 = 0$ proved in Step 2 of Lemma 1. The subsequent proof of convergence to the attractor z^* proceeds in the same way as the proof for Case (C2).

4.4.3. Proof of Objective 2 (O2)

Since the hand hull \mathcal{D} does not appear in \mathcal{R}_0 or \mathcal{R}_2 (see the visualized sets \mathcal{R}_0 and \mathcal{R}_2 in Figure 8 (b) and their definitions detailed in Table A.8), it is sufficient to examine the penetration between the hand hull and the temporal evolution of Eq. (8) with the initial state $z(0) \in \mathcal{R}_1$.

Theorem 2. Consider the dynamical system Eq. (5). Let $z(0) \in \mathcal{R}_1$ be the initial state outside or on the hand hull \mathcal{D} . Then, for any $t \geq 0$, the temporal evolution z(t) in terms of g(z(t)) does not penetrate \mathcal{D} (Definition 1).

Proof. To ensure impenetrability, it is sufficient to show for every state at the hand hull's boundary, i.e., $z_b = \{z \in \mathbb{R}^b \cap \mathbb{R}^1\}$, the

14

velocity vector $\mathbf{g}(z_b)$ Eq. (5) is either directed away or perpendicular to the normal vector $\mathbf{n}(z_b)$ Eq. (B.2) pointing outwards of the hand hull \mathcal{D} , i.e., $\mathbf{n}^{\top}(z_b)\mathbf{g}(z_b) \geq 0$, which is stated in [55, 56, 57].

Consider the boundary set z_b . By design, the velocity vector Eq. (5) for every z_b has the same direction of the tangent vector, i.e., $\mathbf{g}(z_b) = -\|\mathbf{A}_{\mathscr{N}}(z_b - z^*)\|\mathbf{e}(z_b)$. This is visualized in the left column of Figure 9 (a), where the green vector $\mathbf{g}(z_b)$ aligns with the orange vector $\mathbf{e}(z_b)$. With the normal vector of hand hull at the boundary point $\mathbf{n}(z_b)$, i.e., Eq. (B.2) being orthogonal to the target vector $\mathbf{e}(z_b)$, we have

$$\mathbf{n}^{\top}(z_b)\mathbf{g}(z_b) = -\|\mathbf{A}_{\mathscr{I}}(z_b - z^{\star})\|\underbrace{\mathbf{n}^{\top}(z_b)\mathbf{e}(z_b)}_{=0} = 0,$$
 (31)

which concludes the proof.

5. Finger Motion Generation

We generate reactive finger motions using a object-state-dependent transition function, $\epsilon(x) \in [0,1]$, that smoothly interpolates between the hand cage configuration $q_{f,o}$ (detailed in Section 5.1) and power-grasp configuration $q_{f,d}$ (assumed to be given see Remark 1) based on the object-to-attractor distance $||x-x^*||$. This transition is visualized in Figure 13. The resulting finger joint reference

$$\mathbf{q}_{f,r}(\mathbf{x}) = \epsilon(\mathbf{x}) \cdot \mathbf{q}_{f,d} + (1 - \epsilon(\mathbf{x})) \cdot \mathbf{q}_{f,o}, \tag{32}$$

is sent to the finger motion controller (see [44]), with signal flow depicted in Figure 3. The transition function $\epsilon(x)$ in Eq. (32) is designed as

$$\epsilon(\mathbf{x}) = \exp\left(-\left[(\mathbf{x} - \mathbf{x}^{\star})^{T} \mathbf{Q}_{f}(\mathbf{x} - \mathbf{x}^{\star})\right]\right),\tag{33}$$

where $Q_f > 0$ is a positive definite constant matrix that governs the rate of grip aperture (i.e., finger span) relative to changes in the object-to-attractor distance. The matrix Q_f is chosen heuristically ensuring the object enters the hand cage before the fingers close. As results of Eq. (33), as the object moves further away ($||x-x^\star|| \to c$, recalling $x \in B(x^\star,c)$), $\epsilon \to 0$, and the reference becomes the hand-cage configuration, $q_{f,r} \to q_{f,o}$. Conversely, when the object is close to the attractor $||x-x^\star|| \to 0$, we have $\epsilon \to 1$, and the reference Eq. (32) transitions to the final power-grasp configuration, $q_{f,r} \to q_{f,d}$.

Remark 7. The design of Q_f is further affected by uncertainties in object pose estimation, which arises from visual feedback and the effect of finger joint friction in practice.

5.1. Choosing Hand-Cage Configuration

The hand-cage configuration $q_{f,o}$ represents the finger's posture in the approaching phase. While there is no strict mathematical definition for this configuration—owing to variations in multi-fingered hand kinematics and dependence on object shape—the primary consideration is enabling the hand to geometrically "scoop up" the object more effectively during the approach. A common choice is a bowl-like shape, where the four

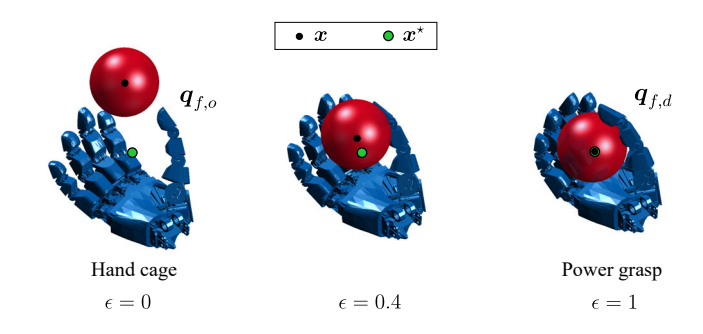


Figure 13: The transition function $\epsilon(x)$ smoothly interpolates between the hand-cage and power-grasp configurations.

fingers (index to little fingers) and the thumb create a smooth, concave space around the palm. As a guideline for creating this bowl-shape cage, we use a five-fingered humanoid hand with 20 DoFs (4 DoFs per finger: 3 for flexion/extension and 1 for ab/adduction) as an example:

- No ab/adduction but with minor flexion at the base joint for the index to little fingers and significant thumb abduction at the base joint;
- Ensure each finger joint configuration is lower-bounded, cf. Figure 12.

This configuration is illustrated in Figure 14 (a). Figures Figure 14 (b) to (d) present three non-hand-cage finger configurations for $q_{f,o}$, including (b) irregular finger positioning that fails to form a coherent cage, (c) an abducted thumb that prevents cage formation, and (d) an irregular finger arrangement resulting in two small, disjointed cages.

6. Experimental Validation, Simulation Study and Discussion

We conducted three types of experiments to evaluate whether FF meets our objectives. Moreover, we will highlight the experimental insights and address the framework's practical strengths and limitations. The experiments are designed as follows:

(1) **Stationary tabletop object**: The robot is tasked with grasping a stationary bottle on a table. The object is placed at random locations and heights.

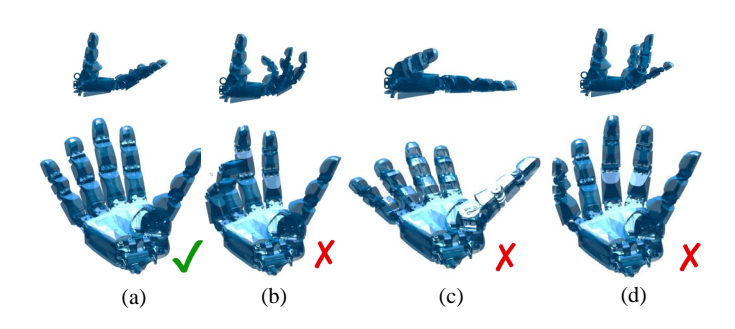


Figure 14: (a): The open hand as hand-cage configuration. (b-d): non-hand-cage finger configurations

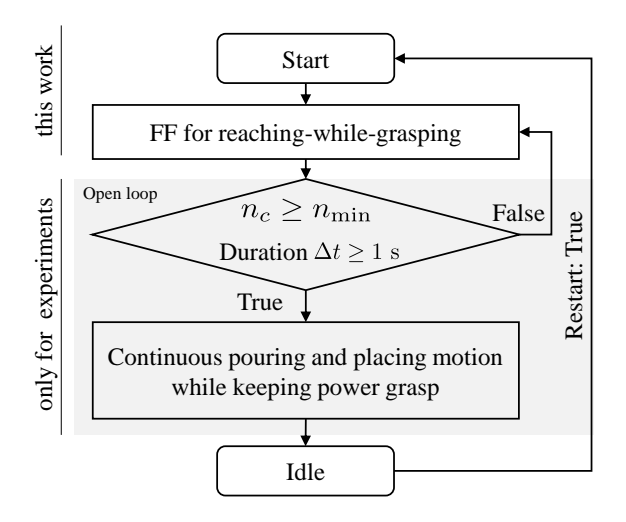


Figure 15: The framework in Figure 3 is followed by the continuous pouring motion used for further verifying the grasp stability, only used in experimental validations. The used parameters are listed in Section Appendix D.2.

(2) **Unpredictably spatially moving object**: The robot is required to grasp a bottle swinging on a rope, where external disturbances cause random motions.

(3) Interactive and adversarial human-to-robot handover:

The robot must grasp a bottle handed over by a human. In this scenario, two distinct cases are considered: the human may act cooperatively or adversarially, subjecting the handover to additional disturbances or making evasive motions.

In all experiments, we chose a ketchup bottle as our test object with a homogeneous mass distribution of 500 g, with 30 cm height and 5 cm diameter. Its mesh file (OBJ file) is assumed to be known and given to the visual tracker. The ketchup bottle is always within the reachable space of the robot and visible in the camera's field of view.

Grasp stability assessment

Grasp stability is assessed through a pouring motion that smoothly transitions from the final grasp state. The grasp is considered stable if the object remains securely held throughout the entire pouring motion sequence. The flowchart is shown in Figure 15. In practice, when the object is near the attractor, visual pose estimation becomes unreliable due to occlusion between the object and the palm or fingers. To mitigate this, we use estimated joint torque to confirm whether a power grasp has been achieved. Specifically, the condition is met if the estimated external torque satisfies $\tau_{i,\text{ext}} \geq \tau_{i,\text{min}}$ for more than 1 second, and the number of engaged finger joints exceeds a predefined minimum $n_c \ge n_{\min}$. Once this condition is met, the motion transitions to a pouring action with the ketchup bottle to demonstrate a successful grasp. The implementation details are summarized in Section Appendix D.2. It is important to note that all grasp executions are conducted in an open-loop manner after the confirmation.

System Setup

We implemented FF on the right arm $(5 \text{ DoFs})^6$ and the right hand (20 DoFs) on the DLR robot neoDavid [41] with different types of variable stiffness actuators (VSAs) [58]. The used parameters are summarized in Table D.9. The generated two vector references $\dot{q}_{a,r}$ Eq. $(22)^7$, $q_{f,r}$ Eq. (32), are sent to the arm and the finger, respectively. Finger Flow for the arm is implemented within a single Matlab/Simulink model with the ESP controller [42, 43]. Similarly, the vector field for the hand is in a separate model with a cascaded controller consisting of an inner-loop tendon force control and an outer-loop joint-space impedance control. The complete Matlab/Simulink models are compiled to C-Code using code generation, and are running on two real-time PCs at 3 kHz (with Intel® CPU CoreTM i7-1185G7 @ 3.00GHz). The forward kinematics and dynamics model of neoDavid is computed at 1 kHz with the libraries by [59].

The DLR robot *neoDavid* is equipped with an Azure Kinect RGB-D camera mounted in its head (eye-to-hand setup) to detect object locations. Utilizing 3D object meshes and kinematic information, the M3T library ⁸ developed by [45] enables robust estimation of the orientation and translation of articulated rigid bodies. In our experimental setup, the system tracks and estimates the pose of a ketchup bottle with a given OBJ file containing detailed vertex information. We get the bounded object pose feedback (\mathbf{x} and $^{\mathcal{H}}\mathbf{R}_o$ in Figure 3) at 30 Hz, with M3T running on an Intel[®] CoreTM i9-11900K CPU @ 3.50 GHz.

6.1. Experiment 1: Grasping a Stationary Tabletop Object

The ketchup bottle is randomly positioned on a round table with a diameter of 0.8 m, with a 9×9 grid as shown in Figure 17. The table height is adjusted to three levels: 0.90 m, 1.0 m, and 1.1 m. The arm is initialized in random configurations above the table while ensuring that the ketchup bottle is not occluded. We conducted 150 trials, with 50 trials at each table height. Trials were excluded if the visual tracker lost the object tracking of the ketchup bottle during the approaching phase. Selected moments from successful attempts are shown in Figure 20 and failed attempts in Figure 21.

6.1.1. Grasp success rate

The statistical grasping results are presented in Figure 18, where red indicates failed grasps and green represents successful grasps. The success rate is categorized by table height and regions visualized in Figure 19 (a). Overall, the results demonstrate a grasp success rate of 87.3%. As illustrated in Figure 21, re-grasping following a failed attempt was successfully achieved due to the state-dependent nature of FF, enabled by its closed-loop execution. In contrast, during the verification phase (i.e., the pouring motion), the ketchup bottle fell again

⁶The entire right arm has a total of 7 degrees of freedom (DoFs). However, due to the limited range of motion at the wrist, the last two DoFs at the wrist are kept fixed. Additionally, the torso is assumed to remain stationary.

⁷We replace the Jacobian J in Eq. (22) with $J_T \in \mathbb{R}^{3\times 5}$ since only five active joints for the arm are in use.

⁸https://github.com/DLR-RM/3DObjectTracking

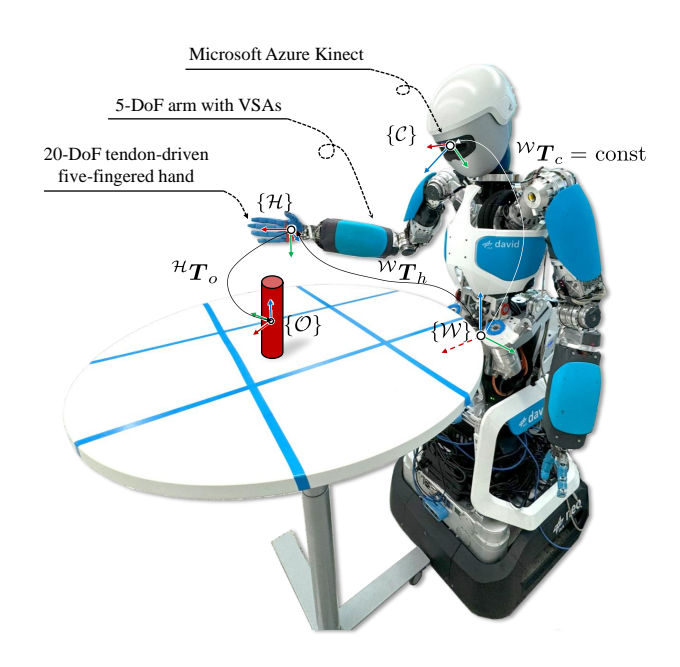


Figure 16: Setup of DLR robot *neoDavid*: The robot is equipped with a Microsoft Azure Kinect camera mounted on its head. The right arm features five active degrees of freedom (DoFs), while the hand includes twenty DoFs. Note that the torso is fixed and not used for the experiment. The following frames are defined: The world frame \mathcal{W} , camera frame \mathcal{C} , hand frame \mathcal{H} , object frame \mathcal{O} . The (x, y, z) or (x_1, x_2, x_3) axes are plotted in red, green, and blue, respectively.

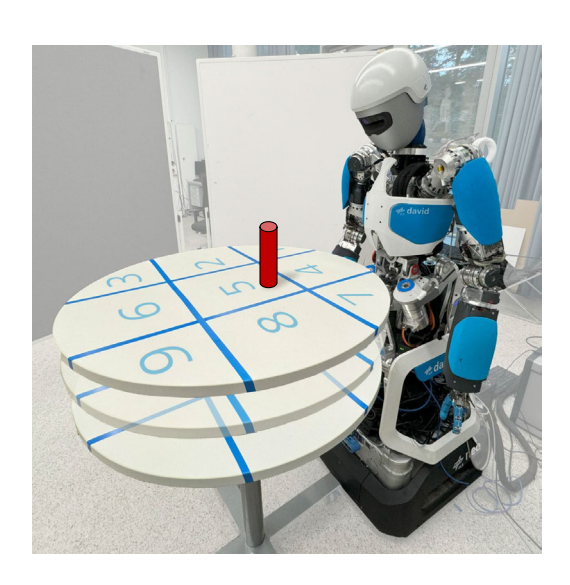
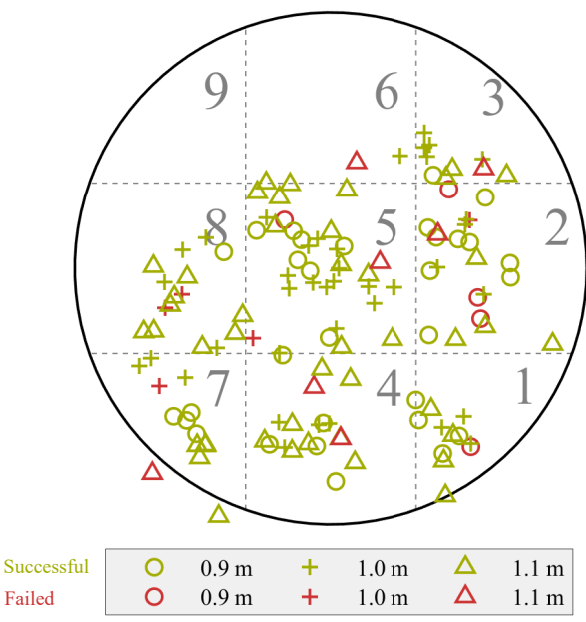


Figure 17: Setup of a stationary tabletop object. The bottle is placed randomly within one of the marked regions (1 to 9) at a height varying between 0.9 m and 1.1 m.



Initial object locations for different table heights

Figure 18: Statistical Results of Experiment 1: An overall success rate of 87.2% was achieved across 132 attempts. Each marker indicates the initial position of the center of a ketchup bottle, projected onto the horizontal plane. Due to perception uncertainties in the world frame, some objects appear projected beyond the table's boundaries.

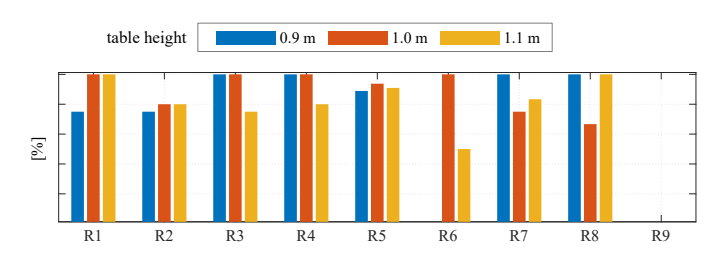


Figure 19: The grasp success rate sorted by regions.

when subjected to the pouring motion, as this operation was performed in an open-loop manner. The shown recovery is challenging due to the arm near the singularity, leading to a misaligned grasp, i.e., a fingertip grasp instead of a power grasp.

6.1.2. Transient object motion in hand cage

A key design idea underlying the semi-tangent flow is allowing sub-optimal grasps for maximizing the overall grasp success rate. This choice stems from the inherent uncertainties arising from unknown object dynamics, perceptual noise, and velocity controller tracking errors, which can lead to unintended object motion within the hand cage. To validate our design idea, we analyze the object's transient motion within the cage across all successful grasping attempts, using both kinematic data and additional video confirmation.

 $^{^9}$ In practice, the transient motion of the object inside the hand cage is also significantly influenced by the surface and geometric properties of both the object and the hand's material covering. These factors are further explored in simulation studies in Section 6.4.

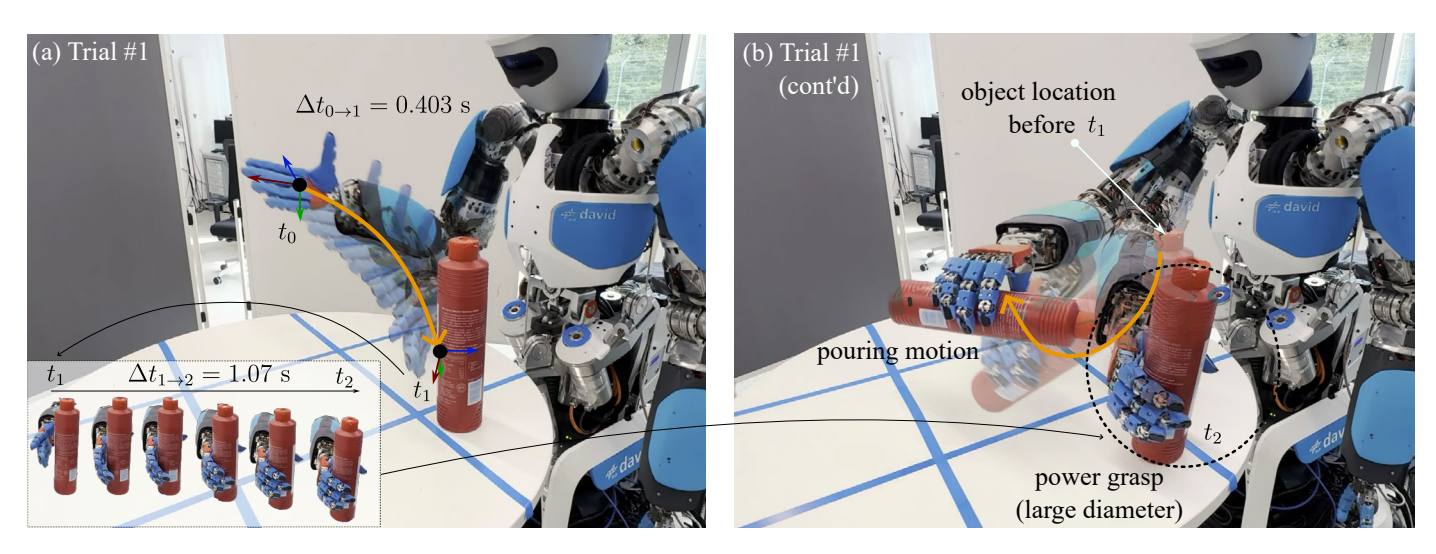


Figure 20: Experiment 1 - selected moments from three successful trials. The orange arrow denotes the trajectory of the hand-fixed attractor P_d . (a) Trial #1: Fast approach within $\Delta t_{0\rightarrow1}=0.403$ second, with orientation converging to the desired pose. Fingers close at the same time. Bottom left: Sequence of finger closures, achieving a power grasp while the hand keeps moving forward and makes the object slide inside the hand cage. See the ketchup bottle's rotation around the vertical axis. (b) Continued Trial #1: Confirmation of a power grasp (large diameter grasp, as classified in [37]) followed by a continuous pouring motion (not the focus of this work).

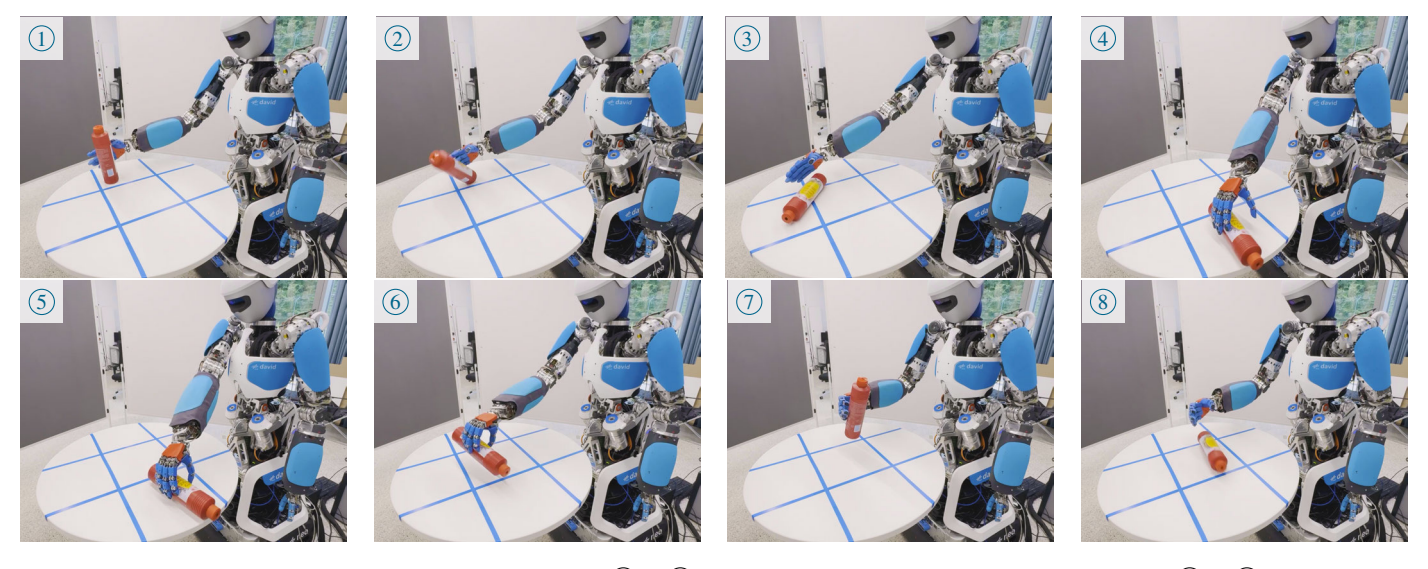


Figure 21: Experiment 1 - analysis of one selected failed attempt. $(1) \rightarrow (2)$: A collision with the thumb causes the object to fall. $(3) \rightarrow (5)$: Grasp recovery attempt: The object continues rolling on the table and temporarily moves out of the robot's reachable space. Meanwhile, due to the closed-loop feature of FF, the arm follows the object's motion. $(5) \rightarrow (6)$: During this time, uncertainties in finger torque estimation lead to an incorrect confirmation of a stable grasp, resulting in a precision grasp as the final grasp state. Note that after this incorrect confirmation, the grasp execution proceeds in an open-loop manner. $(7) \rightarrow (8)$: Pouring motion begins: Although the robot successfully grasps and lifts the object, the dynamic pouring motion causes the object to fall due to the fingertip grasp. Since the grasp is executed in an open loop, the failed grasp cannot be recovered.

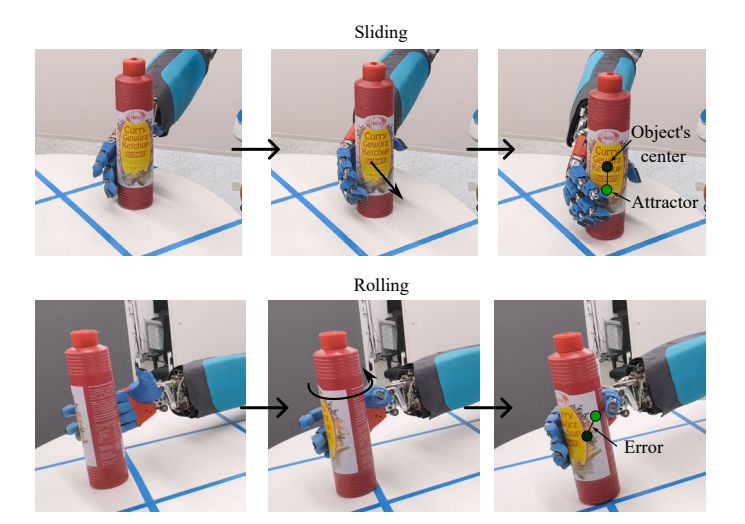


Figure 22: Object in-cage motion: sliding and rolling. The error is parameterized by the norm distance of the object's center to the attractor.

Our analysis reveals that the bottle exhibits either sliding or rolling motion toward an in-cage attractor when the hand continues to push the object inward while the fingers are closing, see Figure 22. The distinction between these two behaviors lies in whether the object undergoes significant rotation about its principal axis. As summarized in Table 1, rolling occurs in 57 % of all cases, often when the arm is near a singular configuration, resulting in reduced hand motion range and allowing the fingers to hook the object into the cage. This alignment facilitates a smoother and stable contact formation, as opposed to an abrupt, impact-like interaction. This leads to a smaller distance error between the object's center and the attractor at the moment of starting of pouring motion. In contrast, sliding occurs in 43 % of trials, typically when the object's center aligns closely with the fixed axis upon entering the hand cage. Despite having sub-optimal grasps during grasp establishment, these observations have demonstrated that our method achieves a satisfactory grasp success rate.

Table 1: In-cage bottle motion for all successful attempts.

Percentage	Sliding: 43 %	Rolling: 57 %
Distance to attractor	3.2 ± 2.5 [cm]	2.7 ± 1.8 [cm]

6.1.3. Failure analysis

We have observed the following causes for the failed 13% (17 of 132) of total grasp attempts. In general, failed attempts are caused by several factors at the same time.

During the approach phase, collisions occur when the thumb slides around or sticks to the object's surface (14/17). Most failed attempts arise from uncertainties in elastic finger position sensing or execution, leading to an inaccurate hand hull approximation. In particular, the error for the thumb will frequently cause collisions. Our used DLR robot *neoDavid* is implemented with a tendon-driven elastic hand.

While the approximated hand hull incorporates a margin to

handle sensing uncertainties by covering all potential finger positions, the uncertainty in elastic finger position estimation remains significantly higher than that of rigid fingers with direct joint position measurement or the rigid tendon with a more accurate model of position estimation. Besides, the silicon cover has the advantage of providing high friction even if the grasp state is imperfect; see the intermediate grasp in Figure 21 (c). However, it can also prevent necessary adjustments that FF provides, such as rolling or sliding of the object within the hand cage, leading to the losing grasp control of the object. As a result, the object may fall, even if it has a smooth surface like a plastic ketchup bottle.

The start of the pouring motion in Figure 15 was incorrectly confirmed (5/17). The joint torque for the tendon-driven hand is estimated based on the tendon force calibration with a tendon-to-joint Jacobian matrix; see details in [44, 60]. Compared to the finger, which implemented a joint torque sensor [61] or tactile sensor over the fingertip, the tendon force will be prone to introduce higher uncertainties in joint torque static bias, which merely depends on finger configurations and stiction effects on the tendons, particularly the thumb's base joint. The erroneous estimated joint torque condition fulfills the condition illustrated in Figure 15, while the stable grasp is still not yet established. The motion afterward is executed in an open-loop manner. Hence, the grasp attempt will most likely fail. Getting a reliable grasp state to ensure a reliable transition to the following motion is out of the scope of this work.

6.2. Experiment 2: Grasping an Unpredictably Moving Object

Unlike Experiment 1, this test introduces the following key challenges: 1) Unpredictably moving motion due to continuously imposed disturbances on the swinging bottle. 2) Limited object tracking rate: The vision tracking operates at a frequency of 30 Hz, which limits the tracking accuracy for objects moving at higher speeds. 3) Uncertainty in visual pose feedback: The object's pose feedback may be imprecise due to unpredictable instantaneous occlusions caused by the robot arm or finger movements.

We keep disturbing the swinging bottle in a random direction with random amplitude persistently, which aims to cause up to 0.8 m/s of the object's Cartesian velocity in the world frame. After each successful grasp of the bottle, we will restart and continue the test. The entire test lasts for 20 minutes.

Figure 23 presents one successful catch of a moving bottle, highlighting key moments with corresponding timestamps. By design, the velocity amplitude in Eq. (18) is preserved relative to the linear field in Eq. (9), increasing velocity norm as the object moves further from the hand (attractor). The fast bottle's motion presents a significant challenge, as the robot often fails to respond in time. In Figure 23 ② to ⑤, the bottle collides with the palm and bounces out of the hand cage before any reactive action can be performed. This limitation arises from the camera's restricted frame rate, which supports video streaming at a maximum of 30 Hz. To mitigate this issue, incorporating predictions of the object's motion $\chi_o \neq 0$ will improve responsiveness if the provided feedback signal has low delay and low noise.

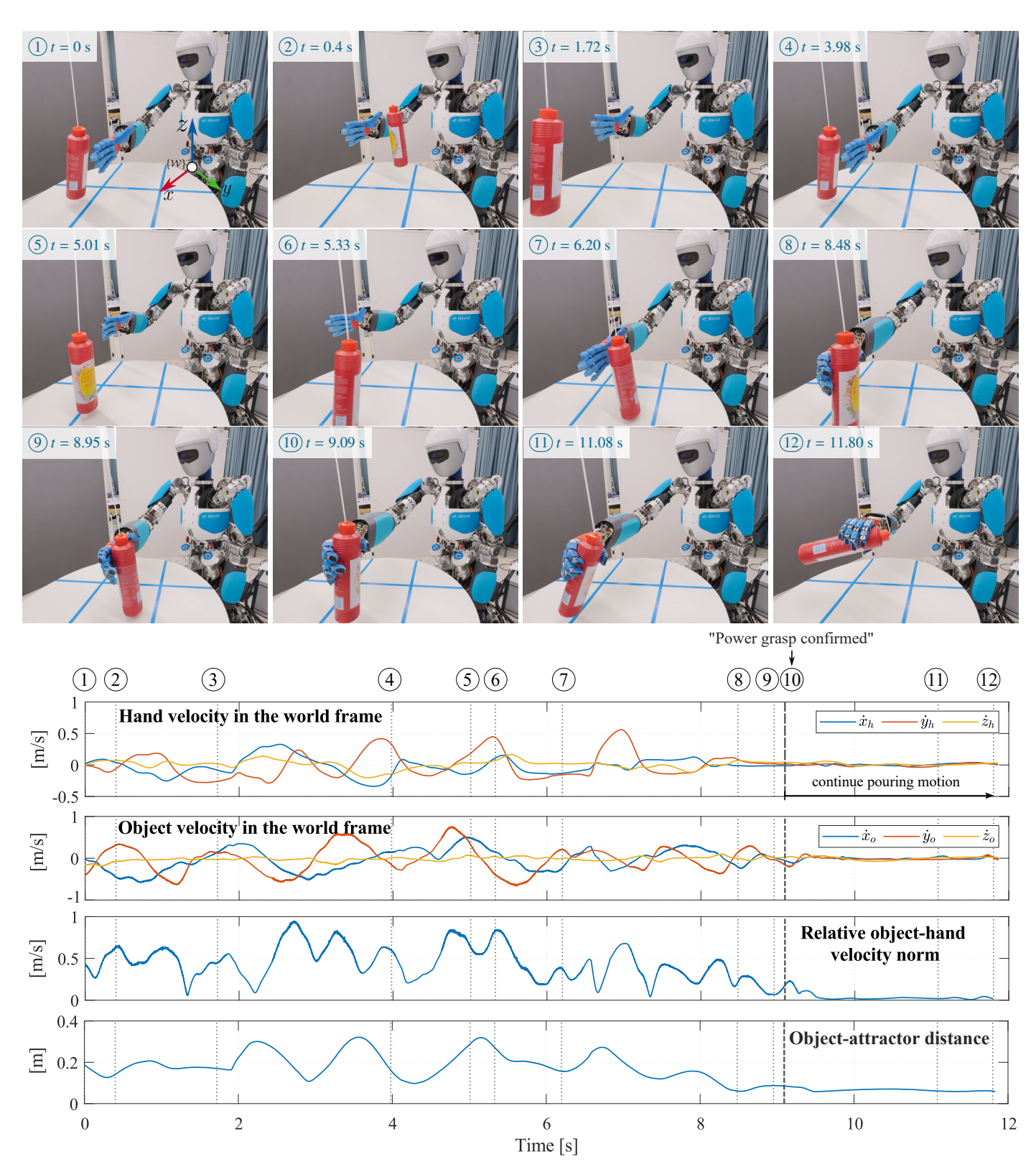


Figure 23: Experiment 2: One of the trials for grasping a moving bottle: The bottle is suspended on the rope, which is continuously disturbed. The timestamp for each photo in the sequence is indicated at the top left of each frame. (1): The object moves behind the thumb, prompting the hand to move away to avoid a collision. (2) \rightarrow (3) ($\Delta t = 1.32$ s): The object moves too quickly for the robot to catch it. (4) \rightarrow (5): The object moves toward the dorsal side, and the hand adjusts its position to avoid hitting the object. (6) \rightarrow (7) ($\Delta t = 0.87$ s): The robot performs a fast approaching. (8) \rightarrow (9): During finger closure, the object slips out of the hand cage slightly, causing the fingers to reopen. (10) \rightarrow (12): Execution of a power grasp and continuous motion for pouring and placing. The relative object-hand distance norm, velocity norm (of vector difference), and their absolute translational velocities in the world frame with corresponding timestamp labels are shown at the bottom.

Statistical results of the bottle's velocity and its distance evolution relative to the attractor across all successful trials are shown in Figure 24 (left). The median peak velocity of the bottle across all trials exceeds 0.7 m/s. Despite the fast speed, the guiding vector flow facilitates real-time adaptation of hand motion and ensures spatial convergence to the attractor. As illustrated in Figure 24 (middle), the bottle is often not fully stationary at the moment of grasp. In most trials, the object-attractor distance converges to approximately 0.02 m, indicating that the bottle's center is well-aligned with the attractor even under dynamic grasping conditions (cf. Figure 24 (right)).

6.3. Experiment 3: Interactive and Adversarial Human-to-Robot Handover of An Object

To evaluate reactive reaching with a human in the loop, a human subject randomly handed the ketchup bottle to the robot while cooperatively or adversarially interacting with the robot arm during the approach phase. The human continuously altered the object's pose, challenging the robot to adapt and complete the grasp. Figure 25 displays the key moments from these interactions.

Although all interactive handover trials were performed continuously, Figure 26 illustrates the final grasp positions (when the stable grasp is confirmed) from all 60 successful handovers (out of 63 total attempts, 95 % success rate). These positions are expressed in the object-fixed coordinate frame. Due to the involvement of human participants in the process, the results are also influenced by their unconscious reactive behaviors, such as adjustments based on humans' tactile feedback from skin contact and visual feedback from observing the robot's interaction with the object. It can be observed that the majority of successful grasps are concentrated in the region above R4 and R5. This area offers optimal robot reachability and provides a stable camera view, which supports accurate object pose estimation during tracking.

Guiding the robot by shared holding an object

In the experiment, when the object is very close to the desired grasp pose (or when the object state lies within the hand hull, which can occur due to visual uncertainties), the reference hand velocity becomes zero. As a result, the closed-loop system behaves similarly to how it would in a zero-gravity environment. This allows the human to freely guide the robotic arm by moving the object, while all fingers maintain a stable grasp throughout the interaction due to our finger generator, see Figure 27.

6.4. Simulation Study

Recent reinforcement learning (RL) approaches have demonstrated reactive grasping with high-DoF hands [17, 62]. However, such methods require extensive offline training in high-fidelity simulators, and the learned policies implicitly rely on horizon-based optimization. Our FF method is a purely model-based, fully reactive controller operating without preview or policy pretraining, and it can be deployed directly on hardware without retraining. Comparing directly to RL methods would

confound the evaluation with differences in training data requirements, simulation-to-reality transfer challenges, and implicit planning horizons, rather than isolating the effect of reactive control without preview. We therefore restrict our baseline comparisons to classic position-based visual seroing (PBVS) and open-loop FF, which align with our problem assumptions and operate under the same model and computation constraints.

To better understand the influence of various parameters, such as those defining the hand hull, the geometric properties of cylindrical objects, and objects' surface roughness, we conduct additional studies in simulation. These are difficult to replicate on physical hardware.

The simulations are built upon the neoDavid setup, using a 7-DoF robotic arm equipped with a 20-DoF multi-fingered hand within the MuJoCo physics engine. To isolate reaching performance from grasping strategy, we use a fixed grasp pose across all trials. A cylindrical object is placed on a tabletop and given a random initial horizontal velocity to induce motion. The cylinder's center of mass is positioned low, near its base, causing it to swing like a Roly-Poly toy. The task is for the robot to reach and grasp this continuously moving object. We initialize the robot hand at various positions around the swinging cylinder, ensuring no initial collision occurs.

6.4.1. Comparison of PBVS, open-loop and closed-loop FF.

PBVS uses a linear control law with a constant gain matrix equivalent to A in Eq. (9). We stack Eq. (9) and the same orientation regulator Eq. (20), and obtain the full 6D body velocity Eq. (21). In contrast, the open-loop FF only utilizes the initial object state $x_0 = x(t = 0)$ at the start of the simulation, ignoring any subsequent motion for all t > 0. Hence, the complete trajectory generated by integrating the dynamic system in Eq. (21) from the initial object state is predetermined.

We run 294 trials for each method and measure success rates based on the object's initial position relative to the dorsal plane of the hand. The final grasp success rate is summarized in Table 2. Each dot in Figure 28 represents the object's center depicted in the hand-fixed coordinate frame, with color coding indicating whether the trial succeeded or failed. Importantly, only the outcome of the first reaching and grasping attempt is considered; subsequent attempts due to the object moving away from the attractor are not counted as successes.

Our results show that PBVS achieves successful attempts *only* when the object initially is located within the region \mathcal{D}_0 directly above the palm. This supports our design choice of maintaining a constant linear flow for region \mathcal{D}_0 . Meanwhile, the open-loop FF yields poor performance in tracking moving objects, as its trajectories rely solely on the initial observation. In contrast, closed-loop FF benefits from continuous finger-state feedback, enabling online adjustment of arm motion to avoid potential finger collisions. As a result, FF achieves the highest overall success rate among the compared methods.

6.4.2. Varying bottle's diameter and surface friction.

We further evaluate the robustness of our method by testing grasp success rates under varying bottle diameters and surface friction levels (i.e., half and twice friction coefficient set-

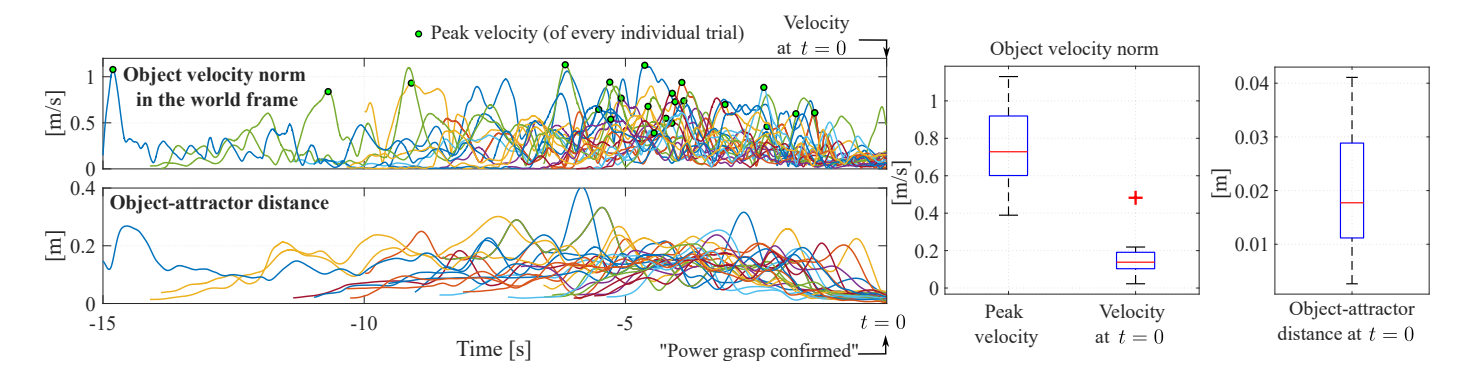


Figure 24: Statistical results of grasping the unpredictably swinging bottle in the space. **Left:** The upper plot shows the norm of the object's absolute translational velocity across all successful attempts, while the lower plot illustrates the time evolution of the distance between the object's center and the attractor over time. Due to the different testing durations, all trials are aligned at t = 0, corresponding to the moment when a stable grasp is confirmed and the pouring motion begins. **Middle:** Box plots of the object's peak velocities and its velocity at t = 0. **Right:** Distance between the object's center and the attractor at t = 0.

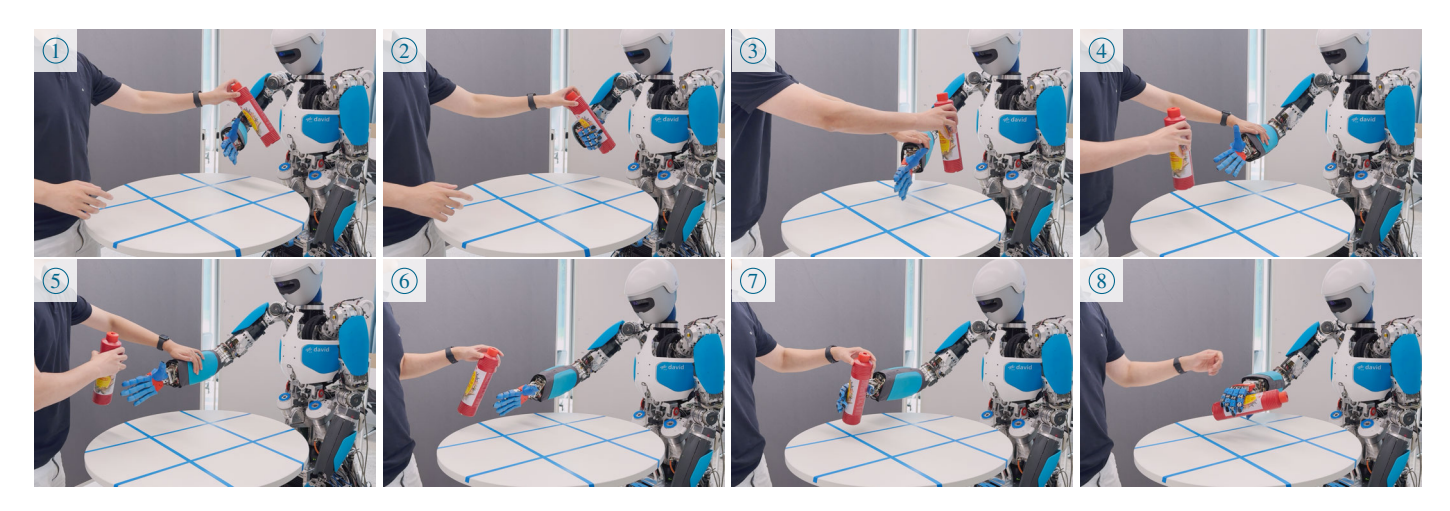


Figure 25: Experiment 3: Interactive and adversarial handover. $(1) \rightarrow (2)$: a stationary object handover. $(3) \rightarrow (5)$: interactive and adversarial handover while the human moves the object. $(6) \rightarrow (7)$: dynamic handover with changing object poses. (8): A stable grasp is detected and confirmed, followed by a pouring motion to verify if the grasp is stable.

Table 2: Grasp success rate in baseline comparison.

Methods	Obj dorsal $(z_3 < 0)$	ect's center at $t = 0$ palmar $(z_3 \ge 0)$	total
PBVS	0/134	62/160	62/294
	(0 %)	(62 %)	(21 %)
Open-	30/134	49/160	79/294
loop FF	(22 %)	(31 %)	(27 %)
FF (ours)	134/134	159/160	293/294
	(100 %)	(99 %)	(99.7 %)

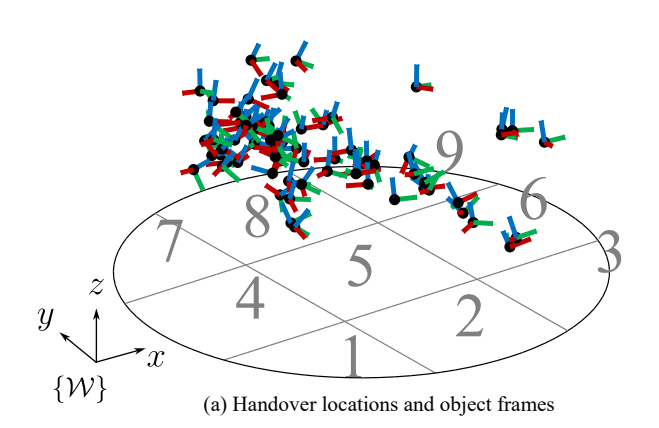
tings (geom/friction) in XML file for the MuJoCo simulator), while keeping the hand hull parameters fixed, see the setup in Figure 29. The hand pose is initialized such that the object's geometric center lies within $x(0) \in \mathcal{D}_0$, with an initial distance of at least 40 cm from the fixed attractor on the hand. Each object is assigned a random initial velocity. For each combination of diameter and friction, we conduct 60 trials, and the results are

summarized in Table 3. We observe that smaller-diameter bottles on low-friction surfaces tend to slide and roll more easily toward the desired attractor, compared to larger-diameter bottles on high-friction surfaces.

The result also supports our design principle based on the "bean-bowl" model, where object motion is guided toward a stable attractor through a finger-aware dynamical system. Conversely, typical failures occur with large-diameter bottles on high-friction surfaces, where finger-bottle stiction prevents effective caging. In these cases, fingers are unable to guide the object toward the palm, often resulting in slippage and loss of the object from the hand.

Table 3: Success rate by varying the bottle's diameter and surface friction.

Friction Diameter	low	high
small large	98 % 89 %	97 % 80 %



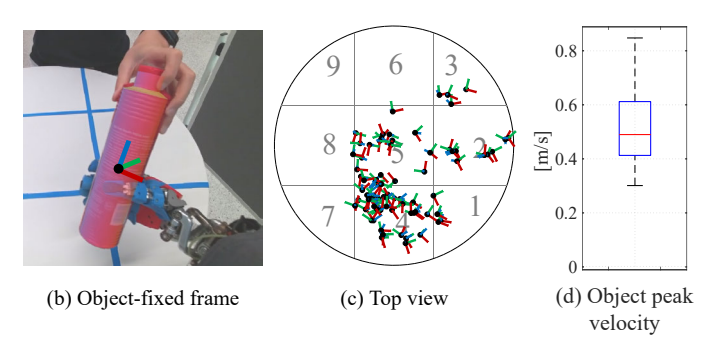


Figure 26: (a) Spatial distribution of the 60 successful handover locations at the moment the power grasp is confirmed (63 total attempts). (b) Handover locations are represented using object-fixed coordinate frames. (c) Top-down view of the handover locations. (d) Object peak (translational) velocity norm across all handovers.

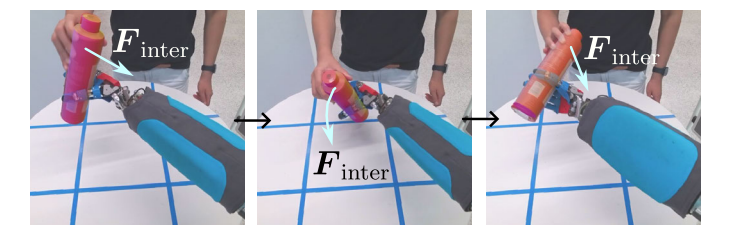


Figure 27: A human and a robot are jointly holding the same object, with the human guiding the robot's movement. The vector \mathbf{F}_{inter} denotes the interaction force that the human exerts.

Table 4: Success rate difference by varying hand hull parameters: Comparison with the success rate (98 %) using the original hand hull.

Thickness	double	half
Difference	-27 %	-9 %
Thumb coverage	partial coverage	over coverage
Difference	-34 %	-19 %

6.4.3. Varying hand hull parameters

We also investigate the impact of modifying key parameters of the hand hull—specifically its thickness (the distance between orange contour depicted in Figure 4 (c)) and the height of the hull near the thumb—which can lead to unintended collisions in real-world scenarios, as illustrated in Figure 21.

By varying these two parameters, we generate different parameterized hand hulls, visualized in Figure 30, and evaluate their performance in grasping the same swinging bottle. For each hand hull, we conduct 102 trials using randomly initialized hand poses that may potentially collide with the thumb, and use the same bottle with randomized initial velocities. We compare the resulting grasp success rates to that of the original hand hull, which achieves a baseline success rate of 98%.

The changes in success rate across different hull designs are summarized in Table 4. In general, any deviation from the optimal hull geometry leads to a drop in the final success rate. Most notably, insufficient thumb coverage results in early collisions between the thumb and the bottle before the object reaches the caging region, leading to the most significant performance degradation. Some failures in the cases of increased hull thickness or excessive thumb coverage are not due to physical collisions, but rather stem from the bottle's center being located within the enlarged hollow region of the hull. In such cases, the reaching motion halts because the object is perceived as having a command velocity of zero inside the hand hull. These findings highlight the importance of accurate thumb coverage and avoiding unnecessary voids in the hull design to improve the final reaching performance.

6.5. Limitations and Outlook

Despite achieving dynamic and reactive grasping capabilities, the current framework has several limitations that offer promising directions for future research.

Non-smooth arm velocity

Firstly, FF generates arm velocity profiles that are not perfectly trackable on actual hardware since the velocity is not smooth when the object state crosses $x_3 = 0$. Smoothing these transitions by designing a continuously differentiable vector field remains an important direction for future work.

Single scalar for finger closure

The current finger-closing strategies are effective for most caging and grasping scenarios, but are governed by a single

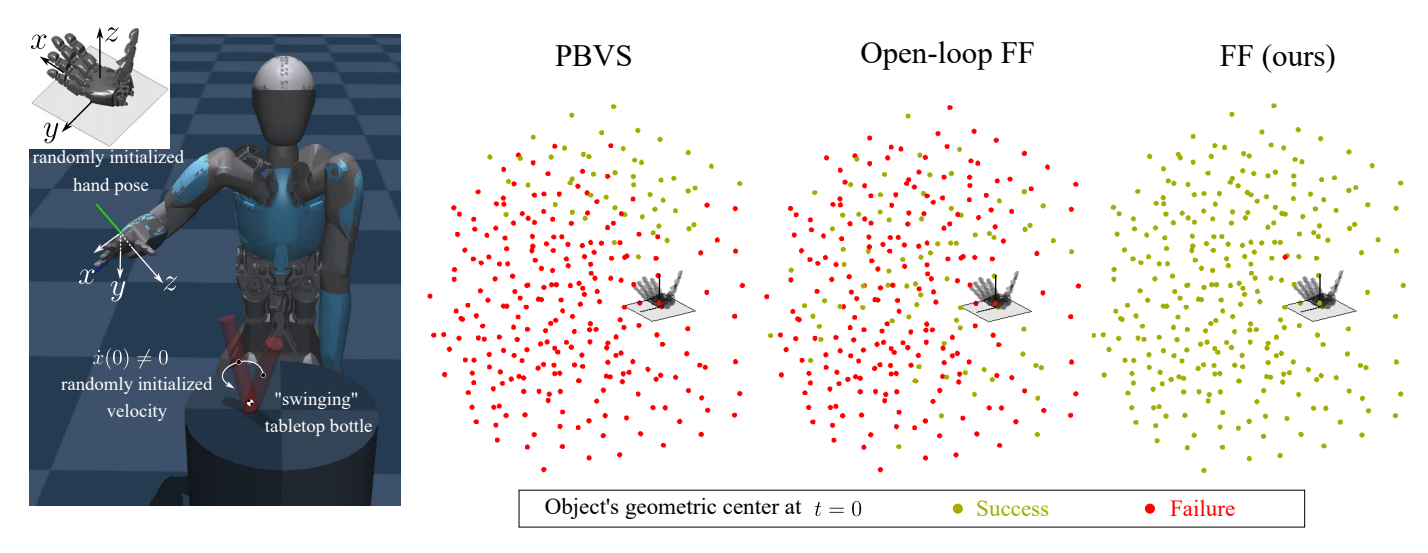


Figure 28: Baseline comparison in simulation. (Left): To evaluate each method, the hand is initialized in 294 randomized poses around a tabletop bottle with a lowered center of mass, causing it to swing persistently due to a randomized initial velocity. (Right): Performance comparison against position-based visual servoing (PBVS) and open-loop FF. Each dot represents the initial position of the object's center in the hand-fixed frame, colored according to the success or failure of each motion generation strategy.

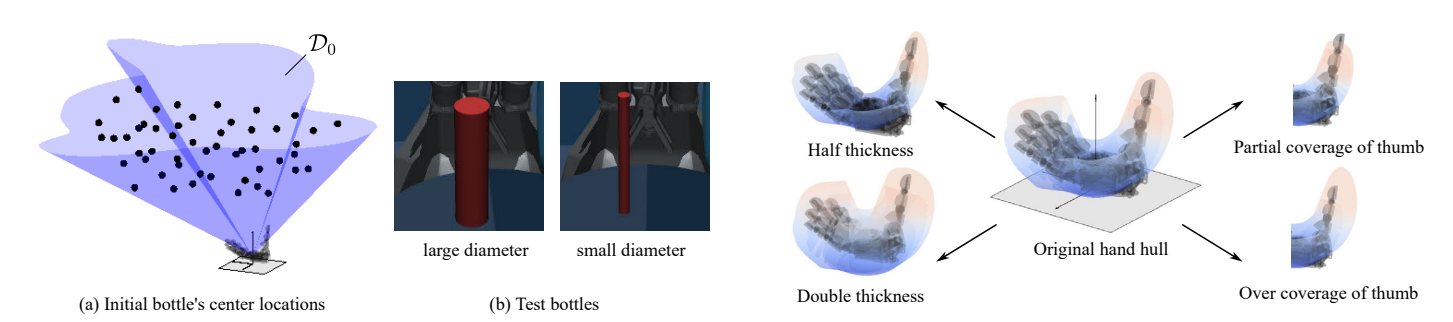


Figure 29: (a): Initial object centers (black dots) are located within region \mathcal{D}_0 , defined as the solid of revolution formed by rotating the tangent line s_1 around the axis, where its slope is rotation-angle dependent. (b): Test bottles with two different diameters used in the experiments.

Figure 30: Varying hand hull thickness and different hand hull coverage for the thumb.

scalar dependent solely on the relative distance. This simplification limits performance in challenging scenarios, such as when the object is of various geometric shapes.

Lack of dynamics modeling

The current FF design does not consider the dynamics of either the object or the robot in the motion planning. For highly dynamic scenarios, such as catching an object with unpredictable motion with peak speeds exceeding 3 m/s, prior knowledge of dynamical parameters like the object's inertia would be essential for refining the FF design. Achieving this, however, would necessitate significant advancements in the hardware setup, including high-speed perception and enhanced control capabilities.

Possible extension to objects in various shapes

The current framework assumes a circular cross-section of constant radius lying on a plane going through the object's geometric center. To generalize this approach to objects with diverse convex shapes, a natural extension is to define dynamic planes that pass through the point on the object's surface closest to the 2D hand hull, rather than the geometric center. On each such plane, the intersection with the object yields a convex 2D shape, which can be tightly enclosed by an ellipse of variable size and orientation. This enables the hand hull to adapt its local thickness dynamically based on the geometry of the enclosing ellipse, replacing the fixed-radius circular assumption.

Adopting this strategy allows us to relax Assumption 1, enhancing the FF's flexibility and geometric fidelity. While using convex hull approximations for objects can suffice for mildly non-convex objects, accurately handling arbitrary geometries—particularly those with pronounced concavities—remains an open challenge. The convex hull, though conservative, may introduce extraneous empty space around the object, potentially leading to undesired behaviors. Addressing such limitations and extending the framework to support complex, non-convex shapes will be the future work.

Proof-of-concept test: Combination with other motion genera-

The semi-tangential flow encodes reaching behavior locally, only when the object is in close proximity to the hand (i.e.,

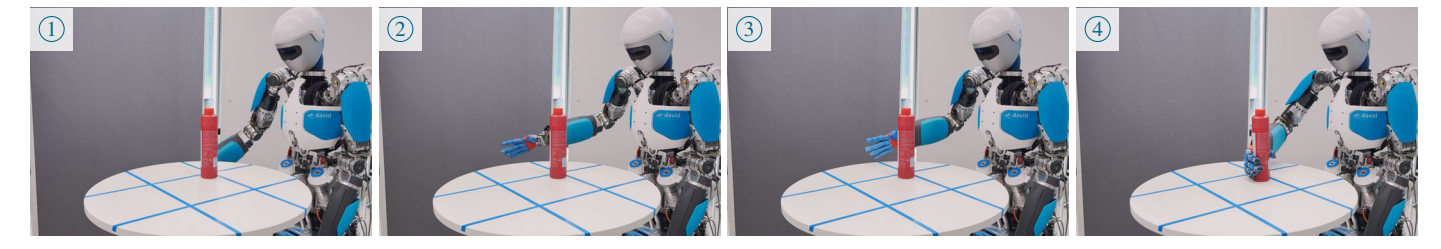


Figure 31: Experiment: Combining FF with Gaussian Mixture Model-based imitation learning (Stable Estimator for Dynamical Systems (SEDS) [63]) to guide the arm around the table. ①: The initial hand position is set below the table. ① \rightarrow ②: With SEDS active, the hand avoids colliding with the table. ② \rightarrow ④: A smooth transition is made to the motion generator with only active FF, enabling a continuous approach and grasp.

within the reactivity margin). When the object is far from the attractor, the flow naturally reverts to a linear form. Leveraging this property, we design a smooth, object-to-palm distance-dependent activation function, such as a sigmoid, to seamlessly blend the FF framework with other motion generators based on the task's requirement.

As a proof of concept, we integrated FF with a Gaussian Mixture Model (GMM)-based imitation learning approach [63], enabling more natural and collision-free motion around environmental constraints such as tables (see Figure 31). The GMM was trained on several collision-avoiding reaching trajectories toward a bottle in the current static workspace. In this setup, the translational hand velocity reference v_r in Eq. (19) is a superposition of velocity outputs of FF and GMM with a smooth, relative-distance-dependent activation function for blending. It means FF is gradually activated only when the object moves near a 30-cm distance sphere from the attractor, while the GMM generates motion primitives outside this range to avoid table collision.

7. Conclusion

Robots traditionally execute sequential "reach-then-grasp" pre-planned motion very often in an open-loop manner. This stepwise approach results in slow, unnatural movements and limits the robot's ability to dynamically respond to environmental changes. Few previous studies address efficient reaching motion generation for robots with multi-fingered hands, which present additional challenges due to their high degrees of freedom and complex meshes, making finger-object collisions a non-negligible issue before achieving the desired grasp state.

In this paper, we proposed Finger Flow, a reactive reach-while-grasp generation framework that utilizes visual and pro-prioceptive feedback to instantaneously provide velocity reference to the lower-level controllers for a robot arm and multifingered hand. FF facilitates the robot to robustly grasp stationary and unpredictably moving objects. By design, FF considers the finger's location and geometry in real-time, continuously guides the hand to avoid collisions with the object during the approaching motion, and adjusts the finger's opening and closure based on the relative pose of the object and hand. This purely state-dependent behavior enabled automatic recovery from failed grasp attempts. We also provided formal proofs of convergence and collision avoidance for the case of grasping a stationary spherical object.

We implemented FF on the DLR robot *neoDavid*, equipped with a multi-fingered hand, and evaluated its performance in a series of fast pick or catch tasks involving stationary and randomly moving test objects. Operating in a closed loop at 3 kHz, FF achieved an over 87% grasp success rate on a stationary object placed at random positions over 130 attempts. Additionally, interactive and adversarial handover experiments demonstrated the robustness and safety of FF during the human-robot interaction.

Currently, FF ensures only piecewise smoothness for arm motion generation while employing simplified finger-closing strategies. Future work involves extending the approach to accommodate diverse object shapes, including concave and irregular forms. Additionally, the current method generates body velocity based on the object-to-hand pose in SO(3) and \mathbb{R}^3 individually rather than addressing the non-Euclidean manifold SE(3) space. Furthermore, practical considerations still need to be addressed, such as actively incorporating sensing uncertainties from visual object feedback and measurements of finger positions and torques. We are confident that the current work has decisively demonstrated that the model-based FF motion generator is not limited to humanoid robots but is equally applicable to manipulators equipped with any multi-fingered hand.

Declaration of generative AI and AI-assisted technologies in the writing process

During the preparation of this work, the authors used ChatGPT-40 for checking grammar and improving language. After using this tool, the authors reviewed and edited the content as needed and take full responsibility for the content of the publication.

Funding

This research did not receive any specific grant from funding agencies in the public, commercial, or not-for-profit sectors.

Declaration of conflicting interests

The author(s) declared no potential conflicts of interest with respect to the research, authorship, and/or publication of this article.

Table A.5: Geometric explanation of different ϕ , u.

Geometric form	φ	и
Ellipse	$\in (0, 2\pi]$	u_0
Arc	$\in (\phi_1, \phi_2)$	u_0
Sector	$\in (\phi_1, \phi_2)$	\in (0, u_0)
Annulus	$\in (\phi_1, \phi_2)$	$\in (u_1, u_2)$

 ϕ_1 and ϕ_2 are starting and ending angles, respectively. u_1 and u_2 are lower and upper bounds or radial scaling.

Appendix A. Hand Hull Generation

We will demonstrate how to approximate the kinematic tree for a single finger on the rotated plane with the angle α , an approach applicable to a human-like multi-fingered hand. We will first illustrate the mapping from the real finger joint position feedback to the estimated finger joint in Section Appendix A.2, which is required for computing the kinematic tree, detailed in Section Appendix A.3.

Appendix A.1. Preliminaries: Rotated and Center-Shifted Ellipses

Consider an ellipse with the center x_c written in a matrix form with distance function $\Gamma(x)$

$$\Gamma(\mathbf{x}) = (\mathbf{x} - \mathbf{x}_c)^{\mathsf{T}} \mathbf{Q} (\mathbf{x} - \mathbf{x}_c) = \Gamma_0 = \text{const} \in \mathbb{R}_0^+, \tag{A.1}$$

where the radius matrix Q can be decomposed as follows

$$\mathbf{Q} = \mathbf{R}(q) \mathbf{\Lambda} \mathbf{R}^{\mathsf{T}}(q) \in \mathbb{R}^{2 \times 2}, \tag{A.2}$$

with

$$\mathbf{R}(q) = \begin{bmatrix} \cos q & -\sin q \\ \sin q & \cos q \end{bmatrix},$$

and the diagonal matrix Λ includes the square inverse of the length for the major and minor axis (l_a, l_b) of an ellipse, written as

$$\mathbf{\Lambda} = \operatorname{diag}(\begin{bmatrix} l_a^{-2} & l_b^{-2} \end{bmatrix}). \tag{A.3}$$

The orthogonal matrix $\mathbf{R}(q) \in SO(2)$ is a rotation matrix with rotation angle q. For later illustration of regions and boundaries in the neighborhood of each finger segment, we utilize the following notation X to parameterize a set of an ellipse's specific sector or arc, which is defined as

$$X(\boldsymbol{x}_c,\boldsymbol{R},\boldsymbol{\Lambda},\phi,u) = \{\boldsymbol{x} \in \mathbb{R}^2 \mid \boldsymbol{x} = \boldsymbol{x}_c + u\boldsymbol{R}\boldsymbol{\Lambda}\begin{bmatrix}\cos\phi\\\sin\phi\end{bmatrix}\}, \quad (\text{A.4})$$

where Λ is expressed in Eq. (A.3), the center x_c with the rotation matrix $R(q) \in SO(2)$, and the parametric angle $\phi \in \mathbb{R}$ and the radial scaling factor $u \in \mathbb{R}^+$ results in different forms of the chosen set, see examples in Table A.5.

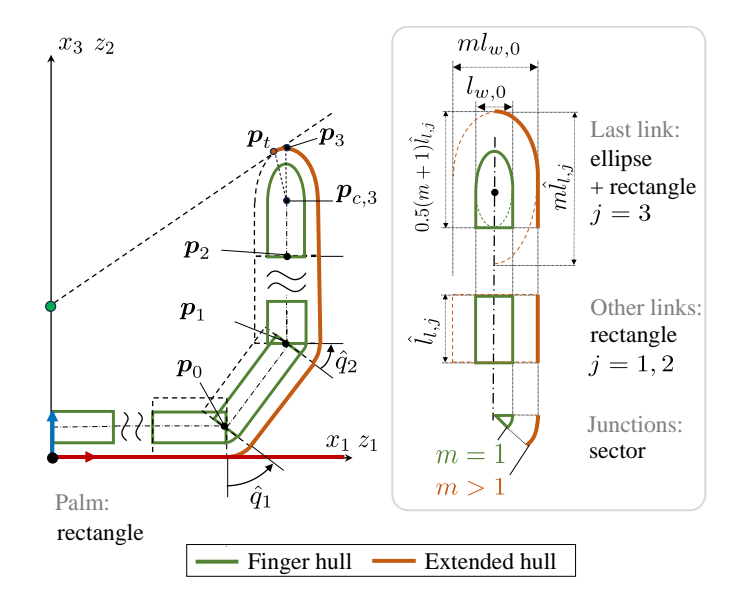


Figure A.32: The estimated finger kinematic chain on each rotated plane. The extended hull is depicted in orange.

Ellipse in A Second-order Polynomial Form

An ellipse in a matrix form Eq. (A.1) can be further expanded into a quadratic form with two scaler arguments x and y, via $x := \begin{bmatrix} x & y \end{bmatrix}^{\mathsf{T}}$

$$a_1x^2 + a_2xy + a_3y^2 + a_4x + a_5y + a_6 = 0.$$
 (A.5)

where coefficients a_1, a_2, a_3 are has following relations with Q Eq. (A.2) given by

$$\mathbf{Q} = \begin{bmatrix} a_1 & \frac{1}{2}a_2\\ \frac{1}{2}a_2 & a_3 \end{bmatrix}. \tag{A.6}$$

The coefficients a_4 , a_5 , a_6 are related to x_c and Γ_0 in Eq. (A.1)

$$\Gamma_0 = -\frac{\det \mathbf{Q}_q}{\det \mathbf{Q}}, \quad \mathbf{x}_c = \mathbf{Q}^{-1} \begin{bmatrix} -\frac{1}{2}a_4\\ -\frac{1}{2}a_5 \end{bmatrix},$$
 (A.7)

where the constant Γ_0 and the center x_c yield to Q_q , given by

$$\mathbf{Q}_q = \begin{bmatrix} a_1 & \frac{1}{2}a_2 & \frac{1}{2}a_4 \\ \frac{1}{2}a_2 & a_3 & \frac{1}{2}a_5 \\ \frac{1}{2}a_4 & \frac{1}{2}a_5 & a_6 \end{bmatrix}.$$

For a non-degenerate conic section $\det \mathbf{Q}_q \neq 0$, \mathbf{Q} is an ellipse if and only if $\det \mathbf{Q} > 0$.

Appendix A.2. Estimation of Finger Configuration and Length

For computational efficiency, the estimated finger has fewer DoFs (n) than the total number of actual fingers' DoFs (n_f) , i.e., $n < n_f$. As an illustrative example, consider a 3-DoF (n = 3) finger modeled as a serial kinematic chain. This finger consists of three flexion/extension joints: the metacarpal, proximal, and distal joints. These joints, denoted as \hat{q}_j , are sequentially indexed as the j-th joint, where j = 1, 2, 3, as shown in Figure A.32. The first link is anchored to a fixed coordinate frame, representing half the radial width of the palm. We

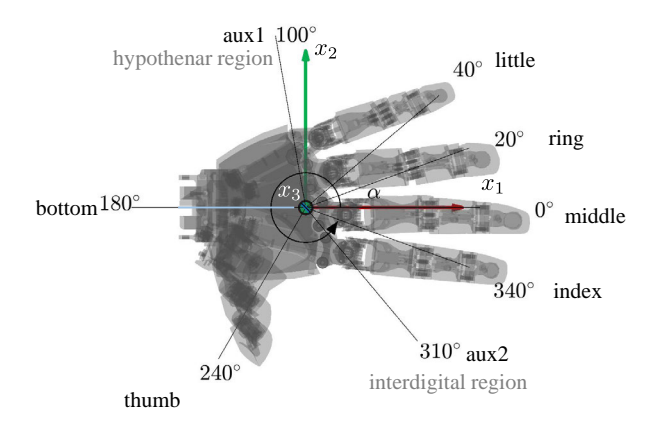


Figure A.33: Top view of rotated planes in different angles α .

employ piecewise 3rd-order polynomials of the rotated plane angle α to estimate the j-th joint configuration \hat{q}_j and the j-th segment length $\hat{l}_{l,j}$ for the kinematic tree. These estimations are expressed as:

$$\hat{q}_{j}(\alpha,q) = p_{q0,j}(q) + p_{q1,j}(q)\alpha + p_{q2,j}(q)\alpha^{2} + p_{q3,j}(q)\alpha^{3},$$
(A.8)

$$\hat{l}_{l,j}(\alpha,q) = p_{l0,j}(q) + p_{l1,j}(q)\alpha + p_{l2,j}(q)\alpha^2 + p_{l3,j}(q)\alpha^3, \ \ (\text{A.9})$$

where the coefficients $p_{(\cdot)0,j},\ldots,p_{(\cdot)3,j}$ are determined based on the boundary conditions for each k-th interval, as outlined in Table A.6. Specifically, the conditions $\hat{q}_j(\alpha_k) = q_j^k$ and $\hat{q}_j(\alpha_{k+1}) = q_j^{k+1}$ yield the following expressions for the coefficients:

$$\begin{split} p_{q0,j} &= q_j^k, \quad p_{q1,j} = q_j^{k+1}, \\ p_{q2,j} &= -\frac{3}{(\alpha_{k+1} - \alpha_k)^2} (q_j^k - q_j^{k+1}), \\ p_{q3,j} &= \frac{2}{(\alpha_{k+1} - \alpha_k)^3} (q_j^k - q_j^{k+1}), \end{split}$$

where q_j^k represents the measured joint position obtained from the hardware. Here, k represents the finger type, specifically $k \in \{\text{thumb, index, middle, ring, little}\}$. Likewise, the estimation of each finger segment length $\hat{l}_{l,j}$ is described by a 3rd-order polynomial in Eq. (A.9). The length and width of each finger segment are provided in Table A.7. As a short notation for Eq. (A.8), we use $\hat{q} = f_{\text{poly3}}(\alpha, q) \in \mathbb{R}^3$ to denote the estimation of finger configuration $\hat{q}_j \in \mathbb{R}^n$, which is lower and upper bounded, i.e., $0 \le q_{\min} \le \hat{q}_j \le q_{\max}$. Figure 12 and Figure 4 (d) illustrate two cases where the estimated joint configuration of the finger violates either the upper or lower bounds. Note that q_{\min} and q_{\max} are not the mechanical range limits of fingers.

Appendix A.3. Estimated Finger Kinematics

As shown in Figure A.32, we use primitive shapes, e.g., rectangles, sectors, and ellipses, to approximate the kinematic tree on each rotated plane. The position of each junction (or finger joint's location), denoted as p_i and each finger segment's center

Table A.6: Boundary conditions for Eq. (A.8) Eq. (A.9) with the rotation angle α in Figure A.33.

α^k [°]	0	20	40	100	180	240	310	340
$\hat{q}^k_j \ \hat{l}^k_{l,j}$	$q_j^{ m mid}$ $l_{l,j}^{ m mid}$	$q_j^{ m ring}$	$q_{j}^{\text{little}} \\ l_{l,j}^{\text{little}}$	q_{\min} $l_{l,j}^{\mathrm{aux}1}$	q_{\min} $l_{l,j}^{ ext{bottom}}$	$q_j^{ m thum}$ m $l_{l,j}^{ m thum}$	$q_{\min}^{ m nb}$ $q_{\min}^{ m nin}$ $l_{l,j}^{ m aux2}$	$q_j^{ m index} \ l_{l,j}^{ m index}$

 $l_{l,j}^k$ is the length of each finger segment. Note that for $\alpha = 100^\circ, 180^\circ, 310^\circ$, we design the radial length l_j^k , where $k = \{\text{aux1, bottom, aux2}\}$, which is designed in terms of the entire distance from the origin to the interdigital or hypothenar regions.

 $p_{c,i}$ are computed by

$$\mathbf{p}_{j} = \mathbf{f}_{fk}(\hat{\mathbf{q}}, \hat{\mathbf{l}}) = \sum_{j=1}^{j} \begin{bmatrix} a_{j} \cos(\sum_{1}^{j} \hat{q}_{j}) \\ a_{j} \sin(\sum_{1}^{j} \hat{q}_{j}) \end{bmatrix} + \mathbf{p}_{0} \in \mathbb{R}^{2}, \quad (A.10)$$

$$\mathbf{p}_{c,j} = \frac{\mathbf{p}_j + \mathbf{p}_{j-1}}{2},\tag{A.11}$$

where the joint angle \hat{q}_j is computed via Eq. (A.8), the p_0 is a static point, a_j is the length of each estimated finger segment, respectively, written as

$$a_j = \begin{cases} \hat{l}_{l,j} & j = 1, 2\\ 0.5(m+1)\hat{l}_{l,j} & j = 3 \end{cases}$$
 (A.12)

where the length $\hat{l}_{l,j}$ is determined using Eq. (A.9). The scalar $m \ge 1$ is calculated as

$$m = \frac{r_o + l_{w,0}}{l_{w\,0}} \tag{A.13}$$

due to Assumption 1, which leads to extending the finger's thickness accordingly. For simplicity, we use the unified finger thickness b_j for all segments, including the palm's thickness, written as $b_j = ml_{w,0}$, $\forall j = 1, 2, 3$. The lengths of all segments, except for the final segment (j = 3), remain unchanged. For the final finger segment, the ratio of the ellipse's major and minor axes is preserved. In Figure A.32, the green and orange external boundaries correspond to cases where m = 1 and m > 1, respectively. The radius matrices for sectorial segments of the finger are computed as

$$\mathbf{Q}_{c,j} = \mathbf{R}(\theta) \operatorname{diag}((0.5ml_{w,0})^{-2}, (0.5ml_{w,0})^{-2}) \mathbf{R}^{\top}(\theta), \quad (A.14)$$

where $\theta = \sum_{i=1}^{j} \hat{q}_{j}$, and for the fingertip's ellipse are expressed as

$$\mathbf{Q}_t = \mathbf{R}(\theta) \operatorname{diag}((0.5ml_{l,3})^{-2}, (0.5ml_{w,0})^{-2}) \mathbf{R}^{\top}(\theta),$$
 (A.15)

where $\theta = \sum_{1}^{3} \hat{q}_{i}$.

Appendix A.4. Closed Forms of Region Definitions

Figure A.34 visualizes the definitions of each region in Table A.8.

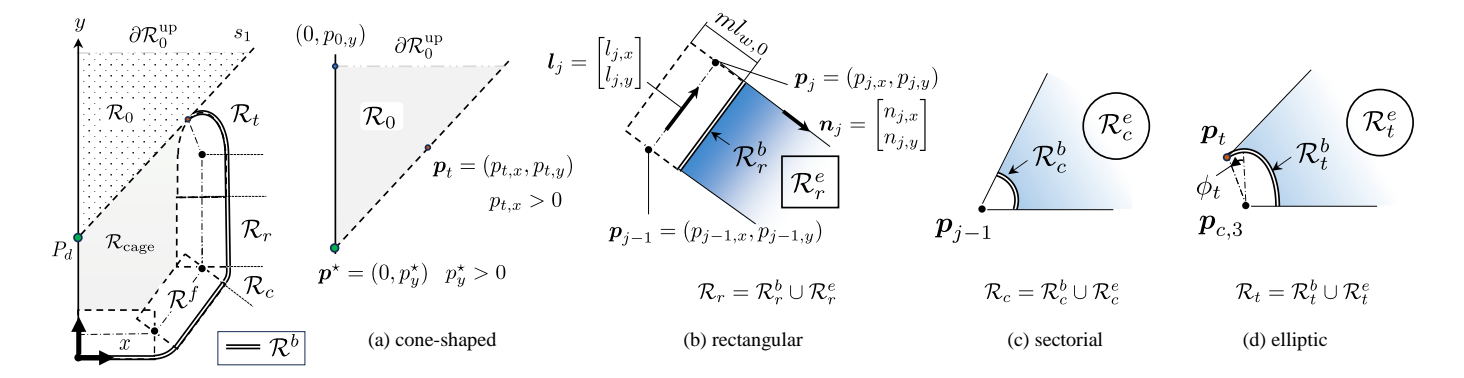


Figure A.34: Visualization of regions in Table A.8.

Table A.7: Finger's length (j = 1, 2, 3) and thickness used for the finger estimation of *neoDavid* hand used in Table A.6.

Var.	Values [m]	Var.	Values [m]
$l_{l,i}^{\text{middle}}$	0.041, 0.041, 0.039	$l_{l,i}^{\text{bottom}}$	0.012, 0.012, 0.010
$l_{l,j}^{ring}$	0.032, 0.032, 0.025	$l_{l,j}^{ m thumb}$	0.050, 0.050, 0.040
$l_{l,j}^{l,j}$ $l_{l,j}^{\mathrm{little}}$	0.028, 0.028 0.022	$l_{l,j}^{\text{aux2}}$ middle	0.004, 0.004, 0.003
$l_{l,j}^{\text{aux 1}}$	0.002, 0.002, 0.002	$l_{l,i}^{\text{middle}}$	0.036, 0.036, 0.028
$l_{w,0}$	0.02	,,	

The cone-shaped set \mathcal{R}_0 :

The set \mathcal{R}_0 , cf. Figure A.34 (a), is enclosed by three half-planes

$$\mathcal{R}_0 = \{ z = (x, y) | x \ge 0, \ y \le p_{0,y}, \ y \ge \frac{p_{t,y} - p_y^*}{p_{t,x}} x + p_y^* \}, \ (A.16)$$

or written as $Gz \leq b$ with

$$\boldsymbol{G} = \begin{bmatrix} -1 & 0 \\ 0 & 1 \\ p_{t,y} - p_{y}^{\star} & -p_{t,x} \end{bmatrix}, \quad \boldsymbol{b} = \begin{bmatrix} 0 \\ p_{0,y} \\ -p_{y}^{\star} p_{t,x} \end{bmatrix}. \tag{A.17}$$

The boundary points of \mathcal{R}_0 are represented as $\partial \mathcal{R}_0^i$, for i = 1, 2, 3, corresponding to cases where the equality in Eq. (A.16) holds. We choose a virtual upper boundary $\partial \mathcal{R}_0^2 := \partial \mathcal{R}_0^{\text{up}}$ such that the \mathcal{R}_0 is a convex set. The computation of the tangent point p_t and line s_1 are shown in Section Appendix B.2.

The rectangular set \mathcal{R}_r :

The semi-open area is represented by three half-planes, cf. Figure A.34 (b), as follows

$$\mathcal{R}_{0} = \{ z = (x, y) \mid n_{j,x} y \ge n_{j,y} (x - p_{j-1,x}) + p_{j-1,y},$$

$$n_{j,x} y \le n_{j,y} (x - p_{j,x}) + p_{j,y},$$

$$l_{j,x} y \le l_{j,y} (x - \bar{p}_{j,x}) + \bar{p}_{j,y}, \},$$
(A.18)

where $\bar{p}_{j,x} = 0.5ml_{w,0}n_{j,x} + p_{j,x}$, and $\bar{p}_{j,y} = 0.5ml_{w,0}n_{j,y} + p_{j,y}$. The set is written as $Gz \le b$ where

$$G = \begin{bmatrix} n_{j,y} & -n_{j,x} \\ n_{j,y} & -n_{j,x} \\ l_{i,y} & -l_{i,x} \end{bmatrix}, \ \boldsymbol{b} = \begin{bmatrix} n_{j,y}p_{j-1,x} - p_{j-1,y} \\ n_{j,y}p_{j,x} - p_{j,y} \\ l_{i,y}\bar{p}_{i,x} - \bar{p}_{i,y} \end{bmatrix}.$$
(A.19)

Appendix B. Tangent Flow

Appendix B.1. Closed Forms for Tangent Flow

As the finger on every rotated plane is approximated using three types of primitive shapes—rectangles, arcs, and ellipses—we outline the method for calculating the tangent flow in the neighborhood of each segment. The closed-form of tangent flow e(z) with given object location z in different regions \mathcal{R}_r , \mathcal{R}_c , and \mathcal{R}_t , cf. Figure B.37 (b)-(d), is given by

$$e(z) = R(\frac{\pi}{2})n(z), \tag{B.1}$$

$$\mathbf{n}(z) = \begin{cases} \mathbf{n}_r & z \in \mathcal{R}_r \\ \mathbf{n}_{Q_{vc,j}} & z \in \mathcal{R}_c \\ \mathbf{n}_{Q_v} & z \in \mathcal{R}_t \end{cases}, \tag{B.2}$$

where the tangent flow Eq. (B.1) can be seen as rotating the outward-pointing normal vector \mathbf{n} Eq. (B.2) of the hand hull \mathcal{D} counterclockwise by $\pi/2$. The normal vector Eq. (B.2) consists of three types depending on the neighborhood regions of finger segments, given by

$$n_r = R(\frac{-\pi}{2}) \frac{p_j - p_{j-1}}{\|p_j - p_{j-1}\|}$$
 (B.3)

$$n_{Q_{vc,j}} = \frac{Q_{vc,j}(z - p_{j-1})}{\|Q_{vc,j}(z - p_{j-1})\|},$$
(B.4)

$$\boldsymbol{n}_{Q_{v}} = \frac{\boldsymbol{Q}_{v}(\boldsymbol{z} - \boldsymbol{p}_{c,v})}{\|\boldsymbol{Q}_{v}(\boldsymbol{z} - \boldsymbol{p}_{c,v})\|},$$
 (B.5)

where n_r is the normal vector of rectangular segments. In Eq. (B.3), p_j denotes the *j*-th finger joint's position (j = 1, 2, 3), and p_c denotes the center of *j*-th link. The normal vectors Eq. (B.4) and Eq. (B.5), respectively, are for the *j*-th sector segment and the last elliptic segment. The radius matrix $Q_{vc,j}$ in Eq. (B.4) is given by

$$\mathbf{Q}_{vc,i} = \mathbf{R}(\theta) \operatorname{diag}((r_{vc})^{-2}, (r_{vc})^{-2}) \mathbf{R}^{\top}(\theta),$$
 (B.6)

where $\theta = \sum_{1}^{j} \hat{q}_{j}$, and p_{j} is given in Eq. (A.10). The distance $r_{vc} = ||z - p_{c,v}||$ is visualized in Figure B.37 (d). Near the fingertip \mathcal{R}_{t} , the tangent flow aligns with the tangent vector of a virtual

Table A.8: Definition of sets in the neighborhood of hand hull \mathcal{D} , depicted in Figure A.34.

Symbol	Category	Set Definition
\mathcal{R}^b_r	Rectangular boundary	$\{z \in \Omega_z \mid G_{[3]}^{\top} z = b_{[3]}, G_{[1:2]} z < b_{[1:2]}\} \text{ Eq. (A.19)}$
\mathcal{R}^b_c	Circular boundary	$X(\mathbf{p}_j, \mathbf{R}(-\sum_{i=1}^{j} q_i), \text{diag}([l_{a,i}^{-2}, l_{b,i}^{-2}]), [-\frac{\pi}{2} - q_j, -\frac{\pi}{2}), 1)$ for $j = 1, 2$, see X in Eq. (A.4).
\mathcal{R}_t^b	Fingertip boundary	$X(\mathbf{p}_{c,3}, \mathbf{R}(-\sum_{i=1}^{3} q_i), \text{diag}([l_{a,3}^{-2}, l_{b,3}^{-2}]), [-\frac{\pi}{2}, \phi_t), 1)$ for $j = 1, 2$. ϕ_t is given in Eq. (B.13).
\mathcal{R}_r^e	Rectangular exterior	$\{z \in \Omega_z \mid Gz < b\}$ Eq. (A.19)
\mathcal{R}_c^e	Circular exterior	$X(\mathbf{p}_{j}, \mathbf{R}(-\sum_{i=1}^{j} q_{i}), \text{diag}([l_{a,i}^{-2}, l_{b,i}^{-2}]), [-\frac{\pi}{2} - q_{j}, -\frac{\pi}{2}), (1, c)), 1 < c < \infty, j = 1, 2$
\mathcal{R}^e_t	Fingertip exterior	$X(\mathbf{p}_{c,3}, \mathbf{R}(-\sum_{i=1}^{3} q_i), \operatorname{diag}([l_{a,3}^{-2}, l_{b,3}^{-2}]), [-\frac{\pi}{2}, \phi_t), (1, c)), 1 < c < \infty.$
\mathcal{R}^b	Boundary	$\{z \in \Omega_z \mid \Gamma(z) = 1\}, \mathcal{R}^b = \mathcal{R}^b_r \cup \mathcal{R}^b_c \cup \mathcal{R}^b_t$
\mathcal{R}^f	Interior set	$\{z\in\Omega_z\mid\Gamma(z)<1\},$
\mathcal{R}_0	Cone set	$\mathcal{R}_0 = \{z \in \Omega_z \mid Gz \le b\}$; the closed-form given in Eq. (A.16).
\mathcal{R}_1	Exterior set	$\{z \in \Omega_z \mid \Gamma(z) > 1\}, \mathcal{R}^1 = \mathcal{R}_r^e \cup \mathcal{R}_c^e \cup \mathcal{R}_t^e$
\mathcal{D}^b	Boundary of hand hull	Surface of revolution of \mathcal{R}^b about x_3 -axis. (If not stated otherwise, a full rotation $[0, 2\pi)$ is assumed.)
\mathcal{D}^f	Interior of hand hull	Solid of revolution of \mathcal{R}^f about x_3 -axis.
\mathcal{D}_0	Spatial region of cone	Solid of revolution of \mathcal{R}_0
\mathcal{D}_1	Spatial region of \mathcal{R}_1	Solid of revolution of \mathcal{R}^1 about x_3 -axis.
\mathcal{D}_2	Region below palm	$\{x \in \Omega \mid x_3 < 0\}$

ellipse. The center $p_{c,v}$ and size Q_v in Eq. (B.5) of this ellipse are chosen to ensure that the tangent flow e remains smooth as it transitions across the switching line s_1 . For more details, refer to Section Appendix B.3.

Appendix B.2. Tangent Line and Point

This section primarily introduces the computation of tangent line s_1 and the tangent point p_t . Consider the tangent line with unknown slope $0 < k < \infty$ passing through the attractor P_d with the coordinate (x_d, y_d) , expressed as

$$y = k(x - x_d) + y_d,$$
 (B.7)

Substitute Eq. (B.7) into Eq. (A.5) leads to quadratic equation of x:

$$A(k)x^{2} + B(k)x + C(k) = 0,$$
 (B.8)

where the coefficients A, B, C are the function of the unknown k are written as $A(k) = a_3k^2 + a_2k + a_1$, $B(k) = a_2(y_d - kx_d) + 2a_3k(y_d - kx_d)$, $C(k) = a_3(y_d - kx_d)^2 + a_5(y_d - kx_d) + a_6$, where a_i , i = 1, ..., 3 are constants from the radius matrix of the last fingertip's ellipse Eq. (A.15) with Eq. (A.7) and Eq. (A.6). The quadratic equation Eq. (B.8) has two identical roots if the line is tangent to the ellipse. This condition implies that the discriminant, $\Delta(k)$, must equal zero for the unknown parameter k, i.e.,

$$\Delta(k) = B^{2}(k) - 4A(k)C(k) = 0 \implies k_{1,2} = f(A, B, C).$$
 (B.9)

Since there are two possible solutions for k, see Figure B.35 (a), we choose the one with the maximal value in Eq. (B.9), i.e.,

$$k = \max(k_1, k_2).$$
 (B.10)

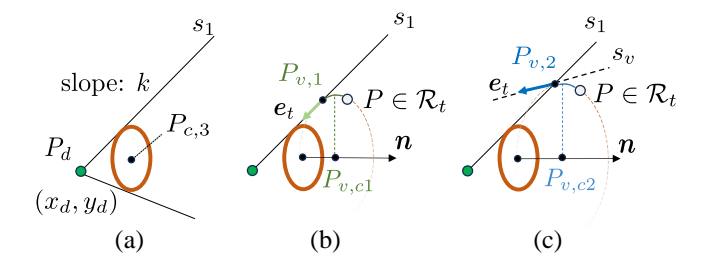


Figure B.35: (a): Two possible tangent lines of the ellipse going through a fixed point outside the ellipse. (b): P on the virtual ellipse (dashed orange line): If $a_1 = a_3$ in Eq. (4), the tangent vector \mathbf{e}_t at $P_{v,1}$ is aligned with s_1 , pointing towards P_d (c): P on the virtual ellipse (dashed orange line): If $a_1 > a_3$ in Eq. (4), the tangent vector \mathbf{e}_t at $P_{v,2}$ is aligned with s_v . s_v is a line has slope $k_v = k \frac{a_3}{a_1}$.

Hence, we get s_1 and $\mathbf{p}_t = (p_{t,x}, p_{t,y})$ computed as

$$p_{t,x} = -\frac{B}{2A}, \quad p_{t,y} = k(p_{t,x} - x_d) + y_d,$$
 (B.11)

$$s_1:\{(x,y)|y-kx-y_d+kx_d=0\}.$$
 (B.12)

The corresponding angle ϕ_t of the tangent point w.r.t. the major axis is computed by

$$\phi_t = \arccos \frac{(p_t - p_{c,3})^{\top} (p_3 - p_{c,3})}{\|p_t - p_{c,3}\| \|p_3 - p_{c,3}\|},$$
 (B.13)

where $\|\boldsymbol{p}_t - \boldsymbol{p}_{c,3}\|$ and $\|\boldsymbol{p}_3 - \boldsymbol{p}_{c,3}\|$ are non-zero.

Appendix B.3. Continuous Tangent Flow Crossing s₁ via Virtual Ellipse

Consider the object state $P \in \mathcal{R}_t$. An arc of the virtual ellipse passing through P represents the temporal evolution of

the object's position at P, as shown in Figure B.35 (b). Let $P_{v,1}$ (whose coordinate p_t) denote the tangent point where the virtual ellipse is tangent to s_1 , and $P_{v,2}$ where the virtual ellipse intersects with s_1 . The objective is to determine the parameters of the virtual ellipse—its center $P_{v,c}$, and radius matrix, Q_{vc} —such that the tangent vector e_t at $P_{v,2}$ (or $P_{v,1}$) transitions smoothly before and after crossing s_1 . Since infinite ellipses satisfy these requirements, we assume

- The ellipse's center $P_{v,c}$ lies on the normal vector \mathbf{n} of the last fingertips' center $P_{c,3}$;
- The virtual ellipse has the same major and minor axes ratio m Eq. (A.13) as the one for the fingertip's ellipse Eq. (A.15).

We have the following case distinction for solving the ellipse, depending on the a_1 and a_3 in $A_{//}$ Eq. (4).

- (I) If $a_1 = a_3$, see Figure B.35 (b), the virtual ellipse is tangent to s_1 .
- (II) If $a_1 > a_3$, see Figure B.35 (c), the virtual ellipse is tangent to s_v , where s_v has slope $k_v = k \frac{a_3}{a_1}$ and intersect with s_1 at $P_{v,2}$.

The ellipse's center P_{vc} , and the radius matrix Q_v in Eq. (B.5) are therefore determined by solving the geometric condition Eq. (B.9) as we mentioned in Section Appendix B.2.

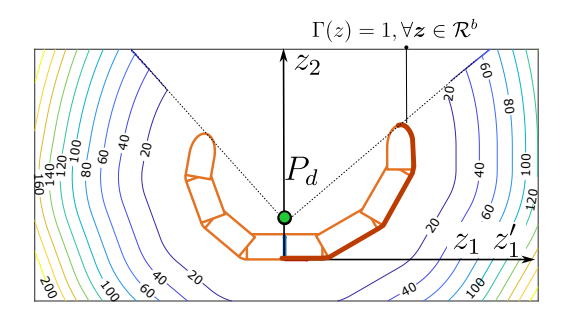


Figure B.36: Isolines of the distance function $\Gamma(z)$. Note that $\Gamma(z)=1$ for $z\in \mathcal{P}^b$

Appendix B.4. State-dependent Transition

The design of a state-dependent transition scalar η is not unique, we choose for example

$$\eta(z) = \frac{1}{2} [1 - \tanh \sigma_1 \cdot (\Gamma(z) - \Gamma_0)] \in [0, 1],$$
(B.14)

where coefficients σ_1 and Γ_0 are interpreted as reactive rate and distance margin for reactivity, respectively, where the distance function $\Gamma(z)$ is state-dependent, which parametrizes the point-to-line, point-to-ellipse metric for representing the distance between the current object state and the planar hand hull \mathcal{R}^b . It is defined as follows

$$\Gamma(z) := \begin{cases} (\frac{2}{ml_{w,0}})^2 [(z - \boldsymbol{p}_j) \wedge \boldsymbol{l}]^2 & z \in \mathcal{R}_r \\ (\frac{2}{ml_{w,0}})^2 (z - \boldsymbol{p}_j)^2 & z \in \mathcal{R}_c \\ (z - \boldsymbol{p}_{c,3})^{\mathsf{T}} \boldsymbol{Q}_t (z - \boldsymbol{p}_{c,3}) & z \in \mathcal{R}_t \end{cases}$$
(B.15)

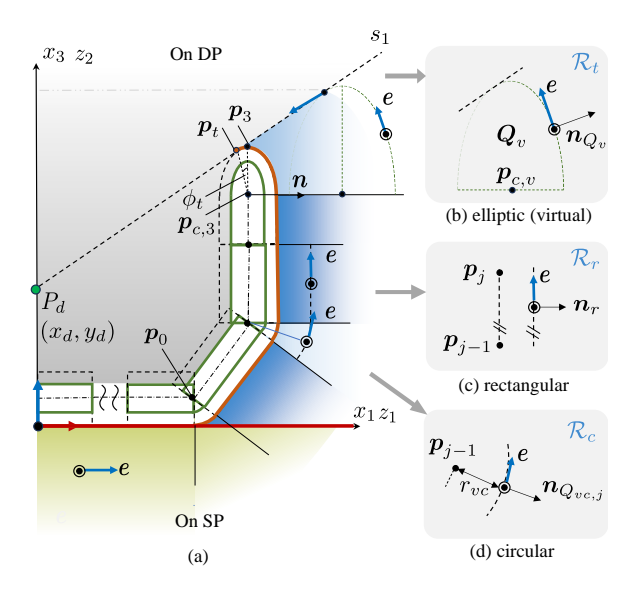


Figure B.37: Tangent flow e (in blue vectors) in different regions.

where $ml_{w,0}$ is the extended finger's thickness, where the m is scaling factor given in Eq. (A.13) due to Assumption 1. The radius matrix Q_t of the fingertip is given in Eq. (A.15). The location of p_j is given in Eq. (A.10) and Eq. (A.11), and visualized in Figure A.32. l represents the unit vector pointing from the j-1-th joint to the j-th joint, computed as $l=\frac{p_j-p_{j-1}}{\|p_j-p_{j-1}\|}$. By design, $\Gamma(z)$ is continuous when z crosses the regions \mathcal{R}_c , \mathcal{R}_r and \mathcal{R}_t . The isolines of Γ are visualized in Figure B.36. The sets \mathcal{R}^b on the hand hull's boundary satisfy $\Gamma(z)=1$. As the object is close to the hand hull's boundary \mathcal{R}^b , $\eta \to 1$. When the object is far away from the P_d , the distance function $\Gamma(z)$ grows quadratically as z moves away from P_d , $\eta \to 0$.

Appendix B.5. Lipschitz Continuity of γ

Lemma 3. For $z \in \mathcal{R}_1$ (or $x \in \mathcal{D}_2$), the rotation angle function $\gamma(z)$ Eq. (6) is (locally) Lipschitz continuous.

Proof. The proof is divided into two main steps:

- 1. Verify whether the function $\gamma(z) = \eta(z) \cdot \gamma_0(z)$ is differentiable within the specified bounded domain.
- 2. Prove that the norm of the derivative of the rotation angle with respect to the state is bounded, i.e., $\|\partial \gamma(z)/\partial z\| \le L_{\gamma}$, where L_{γ} is a positive scalar satisfying $0 < L_{\gamma} < \infty$. By applying the mean value theorem, it follows that $|\gamma(z) \gamma(z')| \le \|\partial \gamma(z)/\partial z\| \le L_{\gamma}$.

Step 1: The transition function $\eta(z)$ Eq. (B.14) is differentiable because it involves the $\tanh(\cdot)$ function, which is smooth and differentiable everywhere. Similarly, $\gamma_0(z)$ Eq. (7) is differentiable due to the following reasons:

1. The term $\operatorname{sgn}(f_{t,w} \wedge e)$ maintains a consistent sign (either positive or negative) within each given domain, ensuring no discontinuities.

- 2. Both $f_{t,w}(z)$ Eq. (3) and e(z) Eq. (B.1) are differentiable by design.
- 3. The norm of $f_{t,w}$ is always nonzero ($||f_{t,w}|| \neq 0$) within the specified domains, avoiding any division-by-zero issues.

Thus, the product $\gamma(z) = \eta(z) \cdot \gamma_0(z)$ is differentiable.

Step 2: The vectors $f_{t,w}$ and e will not be parallel or antiparallel within the specified region due to two key design considerations:

- 1. Anti-parallel alignment is explicitly avoided, as demonstrated by the incorrect finger hull in Figure 12.
- 2. No parallel vectors occur within the given domain. Notably, while $f_{t,w}$ and e are parallel on the tangent line s_1 , this scenario lies outside the domains \mathcal{R}_1 or \mathcal{D}_2 .

Based on the two points discussed above, the function h(z) in Eq. (7), defined as

$$h(z) := \frac{f_{t,w}(z)^{\top} e(z)}{\|f_{t,w}(z)\|},$$
 (B.16)

maps z to a real scalar within the open finite interval (-1,1). The derivative $\partial h(z)/\partial z$ is bounded within the given domain because the dot product of the linear flow $f_{t,w}(z)$ and the tangent flow e(z) results in a quadratic equation. The derivative of this quadratic equation is bounded in the given bounded domain.

Therefore, there exists a finite positive constant $L < \infty$ such that

$$\left\| \frac{\partial \gamma_0(z)}{\partial z} \right\| = \left\| \frac{\partial}{\partial z} \arccos h(z) \right\|$$

$$= \left\| \frac{-1}{\sqrt{1 - h^2(z)}} \frac{\partial h(z)}{\partial z} \right\| \le L$$
(B.17)

where h(z) never reaches ± 1 . Additionally, $\eta(z)$ Eq. (B.14) and its derivative $\partial \eta(z)/\partial z$ are bounded due to the properties of the $\tanh(\cdot)$ function. Combining these results, we conclude that:

$$\begin{split} \left\| \frac{\partial \gamma(z)}{\partial z} \right\| &= \left\| \frac{\partial \eta(z)}{\partial z} \gamma_0(z) + \eta(z) \frac{\partial \gamma_0(z)}{\partial z} \right\| \\ &= \left\| \frac{\partial \eta(z)}{\partial z} \right\| \|\gamma_0(z)\| + \|\eta(z)\| \left\| \frac{\partial \gamma_0(z)}{\partial z} \right\| \le L_{\gamma}, \end{split} \tag{B.18}$$

for all $z \in \mathcal{R}_1$ (or $x \in \mathcal{D}_2$), where $L_{\gamma} > 0$ is a finite constant. This completes the proof.

Appendix C. Invariant Set

Lemma 4. [64, Lemma 3.5] Let P be a polyhedron set for all $z \in \mathbb{R}^n$. One has that P is an invariant set for the continuous system $\dot{z} = Az$, if and only if for every $z \in \partial P$ (i.e., $G_i^{\top}z = b_i$) the following inequality holds: $G_i^{\top}Az \le 0$, i = 1, 2...n.

Proof. See proofs in [64, Lemma 3.5] and [65]. The proof concludes straightforwardly with Nagumo's Theorem [66, Theorem 2.7].

Appendix C.1. Proof: \mathcal{R}_0 is An invariant Set

Proof. Consider the dynamical system Eq. (3) for $z \in \mathcal{R}_0$. For all boundary points $z \in \partial \mathcal{R}_0^i$ Eq. (A.16), cf. Figure A.34 (a), we check whether the inequality $-G_i^T A_{/\!/} \tilde{z} < 0$ holds for each row i of G Eq. (A.17), where i = 1, 2, 3. The error is expressed in a vector form as $\tilde{z} = \text{col}[x, y - p_y^*]$.

(1) For $z \in \partial \mathcal{R}_0^1$: x = 0,

$$-\mathbf{G}_{1}^{\mathsf{T}}\mathbf{A}_{\mathscr{I}}\tilde{\mathbf{z}} = \begin{bmatrix} -1 & 0 \end{bmatrix} \begin{bmatrix} -a_{1}x \\ -a_{3}(y - p_{y}^{\star}) \end{bmatrix} = 0$$
 (C.1)

(2) For $z \in \partial \mathcal{R}_0^2$: $y \ge p_y^*$,

$$-G_2^{\top} A_{\mathscr{I}} \tilde{z} = \begin{bmatrix} 0 & 1 \end{bmatrix} \begin{bmatrix} -a_1 x \\ -a_3 (y - p_y^{\star}) \end{bmatrix}$$

$$= -a_3 (y - p_y^{\star}) \le 0,$$
(C.2)

since $y - p_y^* \ge 0$ holds.

(3) For $z \in s_1(\text{or: } \partial \mathcal{R}_0^3) : y = \frac{p_{t,y} - p_y^*}{p_{t,x}} x + p_y^* \ (y_d = p_y^*, x_d = 0 \text{ in Eq. (B.11), Eq. (B.12)),}$

$$-G_{3}^{\top} A_{\mathscr{I}} \tilde{z} = \begin{bmatrix} p_{t,y} - p_{y}^{\star} & -p_{t,x} \end{bmatrix} \begin{bmatrix} -a_{1}x \\ -a_{3}(y - p_{y}^{\star}) \end{bmatrix}$$

$$= p_{t,x}(-a_{1} + a_{3})(y - p_{y}^{\star}) \leq 0,$$
(C.3)

since $y - p_y^* \ge 0$, $p_{t,x} > 0$ and $a_1 \ge a_3$ (see Eq. (4)) hold.

Hence, the conditions $-G_i^{\mathsf{T}} A_{\mathsf{M}} \tilde{z} \leq 0$ are fulfilled for all boundaries i = 1, 2, 3 required in Lemma 4, which concludes the proof.

Appendix D. Implementation Details in Experimental Validations

Appendix D.1. Used Parameters

The parameters used in Finger Flow for all experimental scenarios are summarized in Table D.9. The definition of each finger joint on each finger (representing positive motion) follows this order: metacarpal (adduction), metacarpal (flexion), proximal (flexion), and distal joint (flexion).

Appendix D.2. Bottle Pouring and Placing Motion

The motion for pouring and placing the bottle is generated using a pre-defined joint-space dynamical system. It transitions between two velocity references in joint space through a smooth, time-dependent blending function given by

$$\dot{\boldsymbol{q}}_{a.c} = k(\tau)\dot{\boldsymbol{q}}_{a.n} + (1 - k(\tau))\dot{\boldsymbol{q}}_{a.r},\tag{D.1}$$

where $\dot{q}_{a,n} = -A_c \cdot (q - q_{a,p})$. Here, $A_c \in \mathbb{R}^{5\times 5}$ is a positive definite diagonal matrix, and $q_{a,p}$ represents the predefined arm joint configuration for the pouring motion. The second term, $\dot{q}_{a,p}$ Eq. (22), is the joint-space velocity reference from the FF. The time-dependent transition function is defined as

Table D.9: Parameters in experimental validations.

Parameters	Values
\mathcal{H}_{R_d}	$\mathbf{R}_{\scriptscriptstyle X}(\pi/2)$,
x^*	$\begin{bmatrix} 0 & 0 & 0.02 \end{bmatrix}$ [m]
A in Eq. (10)	diag(5,5,3)
σ_1 in Eq. (B.14)	0.01
Γ_0 in Eq. (B.14)	150
\boldsymbol{Q}_f in Eq. (33)	diag([80 1 260])
$q_{f,d}$ in Eq. (32)	thumb: $\begin{bmatrix} 0.45 & 0.5 & 0.5 & 0.5 \end{bmatrix}$;
	little: 0 0.7 0.5 0.5 [rad]; other
	fingers: [0 0.5 1.0 1.0] [rad],
$q_{f,o}$ in Eq. (32)	other fingers: $\begin{bmatrix} 0 & 0.524 & 0 & 0 \end{bmatrix}$ [rad],
•	thumb: $\begin{bmatrix} -0.524 & 0.524 & 0 & 0 \end{bmatrix}$ [rad]

 $k(\tau) = \frac{1}{2}[1 + \tanh(5 \cdot (\tau - 1))]$, where $k(\tau) \in (0, 1)$ smoothly transitions from 0 to 1 within 2 seconds. As the final part of the motion, the ketchup bottle is placed at the center of the table. This is achieved by setting an ending arm configuration $q_{a,e}$, while the fingers reopen to the hand-cage configuration $q_{f,o}$. The used parameters in this process are summarized in Table D.10.

Table D.10: Parameters in pouring and placing motion.

Parameters	Values
A_c	$I_{5\times5}$
n_c	6
$ au_{i, ext{min}}$	0.1 [Nm]
$oldsymbol{q}_{a,p}$	$\begin{bmatrix} 25^{\circ} & 40^{\circ} & -10^{\circ} & 70^{\circ} & -60^{\circ} \end{bmatrix}$
$q_{a,e}$	$\begin{bmatrix} 25^{\circ} & 40^{\circ} & -10^{\circ} & 70^{\circ} & 40^{\circ} \end{bmatrix}^{T}$

References

- [1] B. Burgess-Limerick, C. Lehnert, J. Leitner, P. Corke, An architecture for reactive mobile manipulation on-the-move, in: 2023 IEEE International Conference on Robotics and Automation (ICRA), IEEE, 2023, pp. 1623–1629.
- [2] D. Morrison, P. Corke, J. Leitner, Learning robust, realtime, reactive robotic grasping, The International journal of robotics research 39 (2-3) (2020) 183–201.
- [3] P. Rosenberger, A. Cosgun, R. Newbury, J. Kwan, V. Ortenzi, P. Corke, M. Grafinger, Object-independent human-to-robot handovers using real time robotic vision, IEEE Robotics and Automation Letters 6 (1) (2020) 17–23.
- [4] C. Wang, X. Zhang, X. Zang, Y. Liu, G. Ding, W. Yin, J. Zhao, Feature sensing and robotic grasping of objects with uncertain information: A review, Sensors 20 (13) (2020) 3707.

- [5] D. Kappler, F. Meier, J. Issac, J. Mainprice, C. G. Cifuentes, M. Wüthrich, V. Berenz, S. Schaal, N. Ratliff, J. Bohg, Real-time perception meets reactive motion generation, IEEE Robotics and Automation Letters 3 (3) (2018) 1864–1871.
- [6] Q. She, R. Hu, J. Xu, M. Liu, K. Xu, H. Huang, Learning high-dof reaching-and-grasping via dynamic representation of gripper-object interaction, ACM Trans. Graph. 41 (4) (Jul. 2022).
- [7] E. Gat, R. P. Bonnasso, R. Murphy, et al., On three-layer architectures, Artificial intelligence and mobile robots 195 (1998) 210.
- [8] G. Wöhlke, Automatic grasp planning for multifingered robot hands, Journal of Intelligent Manufacturing 3 (1992) 297–316.
- [9] A. Orthey, C. Chamzas, L. E. Kavraki, Sampling-based motion planning: A comparative review, Annual Review of Control, Robotics, and Autonomous Systems 7 (2023).
- [10] V. Mayer, Q. Feng, J. Deng, Y. Shi, Z. Chen, A. Knoll, Ffhnet: Generating multi-fingered robotic grasps for unknown objects in real-time, in: 2022 International Conference on Robotics and Automation (ICRA), IEEE, 2022, pp. 762–769.
- [11] H.-S. Fang, C. Wang, H. Fang, M. Gou, J. Liu, H. Yan, W. Liu, Y. Xie, C. Lu, Anygrasp: Robust and efficient grasp perception in spatial and temporal domains, IEEE Transactions on Robotics (2023).
- [12] H. J. Choi, N. Figueroa, Towards feasible dynamic grasping: Leveraging gaussian process distance field, se (3) equivariance, and riemannian mixture models, in: 2024 IEEE International Conference on Robotics and Automation (ICRA), IEEE, 2024, pp. 6455–6461.
- [13] I. Akinola, J. Xu, S. Song, P. K. Allen, Dynamic grasping with reachability and motion awareness, in: 2021 IEEE/RSJ International Conference on Intelligent Robots and Systems (IROS), IEEE, 2021, pp. 9422–9429.
- [14] S. Kim, A. Shukla, A. Billard, Catching objects in flight, IEEE Transactions on Robotics 30 (5) (2014) 1049–1065.
- [15] S. S. Mirrazavi Salehian, M. Khoramshahi, A. Billard, A dynamical system approach for catching softly a flying object: Theory and experiment, IEEE Transactions on Robotics 32 (2) (2016) 462–471.
- [16] S. Hutchinson, G. Hager, P. Corke, A tutorial on visual servo control, IEEE Transactions on Robotics and Automation 12 (5) (1996) 651–670.
- [17] T. G. W. Lum, M. Matak, V. Makoviychuk, A. Handa, A. Allshire, T. Hermans, N. D. Ratliff, K. Van Wyk, Dextrah-g: Pixels-to-action dexterous arm-hand grasping with geometric fabrics, in: 8th Annual Conference on Robot Learning, 2024.

- [18] K. Hsiao, P. Nangeroni, M. Huber, A. Saxena, A. Y. Ng, Reactive grasping using optical proximity sensors, in: Proceedings of the 2009 IEEE International Conference on Robotics and Automation (ICRA), Kobe, Japan, 2009, pp. 2098–2105.
- [19] S. Ye, K. Suzuki, Y. Suzuki, M. Ishikawa, M. Shimojo, Robust robotic grasping using ir net-structure proximity sensor to handle objects with unknown position and attitude, in: Proceedings of the 2013 IEEE International Conference on Robotics and Automation (ICRA), Karlsruhe, Germany, 2013, pp. 3271–3278.
- [20] Y. Suzuki, K. Koyama, A. Ming, M. Shimojo, Grasping strategy for moving object using net-structure proximity sensor and vision sensor, in: Proceedings of the 2015 IEEE International Conference on Robotics and Automation (ICRA), Seattle, WA, USA, 2015, pp. 1403–1409.
- [21] K. Koyama, M. Shimojo, A. Ming, M. Ishikawa, Integrated control of a multiple-degree-of-freedom hand and arm using a reactive architecture based on high-speed proximity sensing, The International Journal of Robotics Research 38 (14) (2019) 1717–1750.
- [22] Y. Suzuki, R. Yoshida, T. Tsuji, T. Nishimura, T. Watanabe, Grasping strategy for unknown objects based on real-time grasp-stability evaluation using proximity sensing, IEEE Robotics and Automation Letters 7 (4) (2022) 8643–8650.
- [23] O. Khatib, Real-time obstacle avoidance for manipulators and mobile robots, The international journal of robotics research 5 (1) (1986) 90–98.
- [24] C. W. Warren, Global path planning using artificial potential fields, in: 1989 IEEE International Conference on Robotics and Automation, IEEE Computer Society, 1989, pp. 316–317.
- [25] A. Tulbure, O. Khatib, Closing the loop: Real-time perception and control for robust collision avoidance with occluded obstacles, in: 2020 IEEE/RSJ International Conference on Intelligent Robots and Systems (IROS), IEEE, 2020, pp. 5700–5707.
- [26] D. E. Koditschek, E. Rimon, Robot navigation functions on manifolds with boundary, Advances in applied mathematics 11 (4) (1990) 412–442.
- [27] R. Philippsen, R. Siegwart, An interpolated dynamic navigation function, in: Proceedings of the 2005 IEEE international conference on robotics and automation, IEEE, 2005, pp. 3782–3789.
- [28] L. Singh, J. Wen, H. Stephanou, Motion planning and dynamic control of a linked manipulator using modified magnetic fields, in: Proceedings of the 1997 IEEE International Conference on Control Applications, IEEE, 1997, pp. 9–15.

- [29] M. Becker, J. Köhler, S. Haddadin, M. A. Müller, Motion planning using reactive circular fields: A 2d analysis of collision avoidance and goal convergence, IEEE Transactions on Automatic Control (2023).
- [30] S. S. M. Salehian, N. Figueroa, A. Billard, Coordinated multi-arm motion planning: Reaching for moving objects in the face of uncertainty., in: Robotics: Science and Systems, 2016.
- [31] L. Huber, J.-J. Slotine, A. Billard, Avoiding dense and dynamic obstacles in enclosed spaces: Application to moving in crowds, IEEE Transactions on Robotics 38 (5) (2022) 3113–3132.
- [32] C. K. Fourie, N. Figueroa, J. A. Shah, On-manifold strategies for reactive dynamical system modulation with nonconvex obstacles, IEEE Transactions on Robotics (2024).
- [33] A. Shukla, A. Billard, Coupled dynamical system based arm-hand grasping model for learning fast adaptation strategies, Robotics and Autonomous Systems 60 (3) (2012) 424–440.
- [34] H. Qiao, M. Wang, J. Su, S. Jia, R. Li, The concept of "attractive region in environment" and its application in high-precision tasks with low-precision systems, IEEE/ASME Transactions on Mechatronics 20 (5) (2014) 2311–2327.
- [35] G. Wang, K. Ren, A. S. Morgan, K. Hang, Caging in time: A framework for robust object manipulation under uncertainties and limited robot perception, The International Journal of Robotics Research (2025).
- [36] A. Rodriguez, M. T. Mason, S. Ferry, From caging to grasping, The International Journal of Robotics Research 31 (7) (2012) 886–900.
- [37] T. Feix, J. Romero, H.-B. Schmiedmayer, A. M. Dollar, D. Kragic, The grasp taxonomy of human grasp types, IEEE Transactions on Human-Machine Systems 46 (1) (2016) 66–77.
- [38] M. Jeannerod, The timing of natural prehension movements, Journal of motor behavior 16 (3) (1984) 235–254.
- [39] M. Santello, M. Flanders, J. F. Soechting, Patterns of hand motion during grasping and the influence of sensory guidance, Journal of Neuroscience 22 (4) (2002) 1426–1435.
- [40] A. Bicchi, On the closure properties of robotic grasping, The International Journal of Robotics Research 14 (4) (1995) 319–334.
- [41] S. Wolf, C. Hofmann, T. Bahls, H. Maurenbrecher, B. Pleintinger, Modularity in humanoid robot design for flexibility in system structure and application, in: 2023 IEEE-RAS 22nd International Conference on Humanoid Robots (Humanoids), IEEE, 2023, pp. 1–7.

- [42] M. Keppler, D. Lakatos, C. Ott, A. Albu-Schäffer, Elastic structure preserving (esp) control for compliantly actuated robots, IEEE Transactions on Robotics 34 (2) (2018) 317–335.
- [43] X. Meng, M. Keppler, C. Ott, Elastic structure preserving impedance control of bidirectional antagonistic variable stiffness actuation, in: 2021 European Control Conference (ECC), IEEE, 2021, pp. 263–269.
- [44] M. Chalon, Modeling and control of an antagonistically actuated tendon driven anthropomorphic hand, Ph.D. thesis, Mines ParisTech (2013).
- [45] M. Stoiber, M. Elsayed, A. E. Reichert, F. Steidle, D. Lee, R. Triebel, Fusing visual appearance and geometry for multi-modality 6dof object tracking, in: 2023 IEEE/RSJ International Conference on Intelligent Robots and Systems (IROS), IEEE, 2023, pp. 1170–1177.
- [46] M. Malvezzi, G. Gioioso, G. Salvietti, D. Prattichizzo, A. Bicchi, Syngrasp: A matlab toolbox for grasp analysis of human and robotic hands, in: 2013 IEEE International Conference on Robotics and Automation, IEEE, 2013, pp. 1088–1093.
- [47] Y. Xu, W. Wan, J. Zhang, H. Liu, Z. Shan, H. Shen, R. Wang, H. Geng, Y. Weng, J. Chen, et al., Unidexgrasp: Universal robotic dexterous grasping via learning diverse proposal generation and goal-conditioned policy, in: Proceedings of the IEEE/CVF Conference on Computer Vision and Pattern Recognition, 2023, pp. 4737–4746.
- [48] K. A. Stroud, D. J. Booth, Engineering mathematics, Bloomsbury Publishing, 2020.
- [49] E. D. Fasse, J. F. Broenink, A spatial impedance controller for robotic manipulation, IEEE Transactions on Robotics and Automation 13 (4) (1997) 546–556.
- [50] E. D. Fasse, N. Hogan, Control of physical contact and dynamic interaction, in: Robotics Research: The Seventh International Symposium, Springer, 1996, pp. 28–38.
- [51] S. M. LaValle, Planning algorithms, Cambridge university press, 2006.
- [52] A. F. Filippov, Differential equations with discontinuous right-hand side, Matematicheskii sbornik 93 (1) (1960) 99–128.
- [53] S. Sastry, Nonlinear systems: analysis, stability, and control, Vol. 10, Springer Science & Business Media, 2013.
- [54] W. Rudin, et al., Principles of mathematical analysis, Vol. 3, McGraw-hill New York, 1964.
- [55] H. J. S. Feder, J.-J. Slotine, Real-time path planning using harmonic potentials in dynamic environments, in: Proceedings of International Conference on Robotics and Automation, Vol. 1, IEEE, 1997, pp. 874–881.

- [56] S. M. Khansari-Zadeh, A. Billard, A dynamical system approach to realtime obstacle avoidance, Autonomous Robots 32 (2012) 433–454.
- [57] L. Huber, J.-J. Slotine, A. Billard, Avoidance of concave obstacles through rotation of nonlinear dynamics, IEEE Transactions on Robotics (2023).
- [58] S. Wolf, G. Grioli, O. Eiberger, W. Friedl, M. Grebenstein, H. Höppner, E. Burdet, D. G. Caldwell, R. Carloni, M. G. Catalano, D. Lefeber, S. Stramigioli, N. Tsagarakis, M. Van Damme, R. Van Ham, B. Vanderborght, L. C. Visser, A. Bicchi, A. Albu-Schäffer, Variable stiffness actuators: Review on design and components, IEEE/ASME Transactions on Mechatronics 21 (5) (2016) 2418–2430.
- [59] G. Garofalo, C. Ott, A. Albu-Schäffer, On the closed form computation of the dynamic matrices and their differentiations, in: 2013 IEEE/RSJ International Conference on Intelligent Robots and Systems, IEEE, 2013, pp. 2364– 2359.
- [60] G. J. Pollayil, X. Meng, M. Keppler, M. Pfanne, A. Bicchi, C. Ott, Elastic structure preserving impedance control for nonlinearly coupled tendon-driven systems, IEEE Control Systems Letters 6 (2021) 1982–1987.
- [61] J. Butterfaß, M. Grebenstein, H. Liu, G. Hirzinger, Dlrhand ii: Next generation of a dextrous robot hand, in: Proceedings 2001 ICRA. IEEE International Conference on Robotics and Automation (Cat. No. 01CH37164), Vol. 1, IEEE, 2001, pp. 109–114.
- [62] R. Singh, A. Allshire, A. Handa, N. Ratliff, K. Van Wyk, Dextrah-rgb: Visuomotor policies to grasp anything with dexterous hands, arXiv preprint arXiv:2412.01791 (2024).
- [63] S. M. Khansari-Zadeh, A. Billard, Learning stable non-linear dynamical systems with Gaussian mixture models, IEEE Transactions on Robotics (5) (2011) 943–957.
- [64] Z. Horváth, Y. Song, T. Terlaky, A novel unified approach to invariance conditions for a linear dynamical system, Applied Mathematics and Computation 298 (2017) 351– 367.
- [65] F. Blanchini, Set invariance in control, Automatica 35 (11) (1999) 1747–1767.
- [66] M. Nagumo, Über die lage der integralkurven gewöhnlicher differentialgleichungen, Proceedings of the Physico-Mathematical Society of Japan. 3rd Series 24 (1942) 551–559.